ALMA MATER STUDIORUM
UNIVERSITÀ DI BOLOGNA

SCHOOL OF ENGINEERING

SECOND CYCLE MASTER'S DEGREE in
AEROSPACE ENGINEERING
Class LM-20

Analysis of the atmospheric and cryovolcanic properties of Enceladus by radio occultation experiments of Cassini

Thesis in:
Spacecraft Orbital Dynamics and Control

Supervisor:
Prof. MARCO ZANNONI

Co-supervisors:
Prof. PAUL WITHERS
Prof. PAOLO TORTORA

Defended by:
ALESSIO BONACA

ACADEMIC YEAR 2022/2023

Abstract

The proposed work, developed at Boston University, analyzes radio occultation data transmitted by Cassini during two observation of Enceladus, performed in 2006 and in 2010. The aim is to determine electron densities around the satellite and within its water plumes occurring near the South Pole. The implemented methodology involves the combination of frequency data in two bands to reconstruct profiles of total electron content crossed by electromagnetic rays during their propagation. These profiles were then used to calculate local electron density profiles around Enceladus as a function of altitude, using spherical and cylindrical version of the Abel transform. Data for the two occultation revealed to be significantly affected by noise. Correction strategies were tested to improve results, with no meaningful improvements. Investigation of the ionosphere of Saturn revealed that the crossing of this region during experiments did not constitute a relevant source of disturbance. Existing in-situ electron density measurements were used to simulate the theoretically observed effects of these features in radio occultation experiments, which resulted to be smaller than uncertainties. Finally, models for water jet densities were employed to assess an upper value on plume densities observable in the experiment.

Contents

List of Figures

List of Tables

Chapter 1

Introduction

1.1 Thesis outline

The goal of the presented thesis work is to study frequency data for radio occultations performed by Cassini on Enceladus, a moon of Saturn considered potentially habitable for the presence of components associated to life, including water, and internal heat sources, as evidenced by ongoing geological activity. This analysis aims to verify in-situ measurements of densities collected in the plasma environment of Enceladus. Additionally, this study explores the application of radio occultation experiments to unusual environments. In fact, these observations are usually conducted on planetary atmospheres, consisting of narrow regions surrounding the celestial body, while the diffused plasma environment of Enceladus extends for distance scales larger than its diameter.

Radio signals transmitted by Cassini during occultation were affected by Doppler shift, neutral particles, and electrons interacting with electromagnetic waves during their propagation to the Earth. Since Cassini could emit radio signals in three different bands (S-, X-, and Ka-bands), the combination of data for multiple bands, recovered as time sequences of frequencies from the PDS archives, allows for the isolation of the effect of electrons. Results of this combination, after some corrections, are utilized to estimate the total electron content encountered by radio signals during the experiment. Electron density as a function of altitude can then be estimated from total electron content profiles and occultation geometry. Finally, the obtained results are compared with the expected values from existing density measurements and models through integration of electron density along the ray paths.

The next sections of this chapter introduce some theoretical background for radio occultation experiments, a summary of the main findings of Cassini and its radio science equipment, and the main characteristics of Enceladus. Available data for the two occultations of Enceladus as time series of frequencies is shown in chapter 2. Chapter 3 describes the methodology developed to obtain electron density estimates from occultation frequency data. Results of this procedure are illustrated and commented in chapter 4. Finally, a comparison of results with those of other studies is performed in chapter 5, along with some final remarks.

1.2 Principles of radio occultations

Radio occultation is a remote sensing technique which uses radio signals transmitted in such a way to cross a planetary atmosphere before being received. This approach allows for the analysis of the physical properties of that atmosphere. Signals moving in an optical medium experience a refraction effect, proportional to the gradient of the refractive index μ, a property of the optical medium which depends on the gas composition and local density of the atmosphere, defined as the ratio between the speed of light in vacuum and the phase velocity of the electromagnetic wave in the medium. In planetary science, radio occultations are typically performed using a radio wave transmitted by a spacecraft in the vicinity of the celestial body to be studied, and received by a ground antenna, such as a Deep Space Network (DSN) antenna, after having crossed the atmosphere in question. This layout is depicted in Figure 1.1.

The direction of propagation $\hat{l}$ of a radio signal in an optical medium

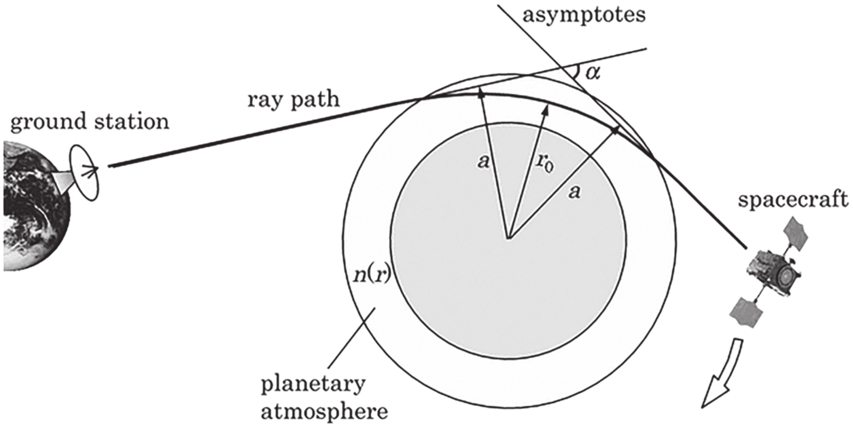

Figure 1.1: Representation of a radio occultation experiment. The bending angle α is increased to obtain a clear picture [19].

is affected as follows [20]:

$$\frac{d}{dl}\left(\mu\hat{l}\right) = \nabla\mu \tag{1.1}$$

Measuring the bending angles experienced by the radio signal during the experiment allows for the estimation of μ in the planetary atmosphere as a function of the altitude, and consequently to infer the main atmospheric properties. Bending angles are derived from frequency measurements since direct observation would be less accurate. Moreover, when observing satellites, the typically low atmospheric densities usually generate deflections too small to be measured. A radio signal transmitted at a frequency f_T is received, after some time, at a different frequency f_R, due to Doppler shift, relativistic effects, and refraction, according to the following relationship:

$$\frac{f_R}{f_T} = \frac{1 - \frac{\bar{V}_R \cdot \hat{n}_R}{c} - \frac{U_R}{c^2} + \frac{V_R^2}{2c^2}}{1 - \frac{\bar{V}_T \cdot \hat{n}_T}{c} - \frac{U_T}{c^2} + \frac{V_T^2}{2c^2}} \tag{1.2}$$

where $\bar{V}_R$ and $\bar{V}_T$ are the velocities of the receiver and of the transmitter with respect to the occulting body in an inertial frame, $\hat{n}_R$ and $\hat{n}_T$ the directions of propagation of the signal at reception and transmission, U_R and U_T the gravitational potentials at the receiver and at the transmitter. If no occultation occurs, the direction of propagation of the signal is not affected and therefore $\hat{n}_R$ and $\hat{n}_T$ coincide: as a result, the calculation of the ideal received frequency $f_{R,id}$ is straightforward once the relative positions of the spacecraft and the ground antenna are known. When radio waves interact with a planetary atmosphere, the received frequency f_R is affected: the frequency residual Δf is defined as the difference between the observed frequency and the one computed in absence of an occultation.

Some assumptions about the surrounding environment are necessary to obtain the refractive index profile as a function of the radial distance R from the center of the celestial body, $\mu(R)$. The hypothesis of spherical symmetry greatly simplifies the geometry of the problem, as the ray propagation would be limited to a plane containing the transmitter, the receiver, and the center of the occulting body. Under this assumption, starting from a time sequence of frequency residuals, time sequences of bending angles α and impact parameters X, defined as the distance of a ray at its point of closest approach to the occulting body, can be calculated from simple geometrical expressions. The resulting $\mu(R)$ is then derived from α and X through an Abel transform.

The hypothesis of spherical symmetry of the refractive environment is adequate for analyzing small satellites, but it does not apply to more complex atmospheres, such as those of gas giants, mainly due to their oblateness and the presence of strong zonal winds. A proper description of the propagation of radio signals in such environments can be obtained using more complex models. For example, Schinder et al. developed a numerical routine which integrates the ray propagation in the atmosphere of an oblate body, defining at each time step a new layer with a constant variation of μ with respect to the acceleration potential, in such a way that the correspondent refraction of the ray is compatible with the measured Δf: the vertical profile $\mu(R)$ is finally computed from the integration of the refractive index variations through all the layers [13].

Once the vertical profile of the refractive index is determined using a specific methodology, it can be used to estimate the physical properties of the atmosphere in question. The refractivity ν, defined as $\nu = \mu - 1$, is the sum of two contributions, respectively from the ionosphere, ν_e, and from the neutral atmosphere, ν_n:

$$\nu = \nu_e + \nu_n \tag{1.3}$$

The ionospheric contribution to the total refractivity is equal to:

$$\nu_e = -\frac{N_e e^2}{8\pi^2 m_e \varepsilon_0 f^2} \tag{1.4}$$

where N_e is the local electron density (electrons per unit volume), e the elementary electric charge, m_e the electron mass, ε_0 the vacuum permittivity, f the frequency of the radio signal. It is worth noting that this effect is frequency dependent. If $\nu_e(R)$ is known, the vertical profile of electron density $N_e(R)$ can be obtained using Equation 1.4. The contribution of neutral atmosphere can be expressed as the sum of contributions from the single gases:

$$\nu_n = \sum_i k_i n_{n,i} \tag{1.5}$$

where k_i and $n_{n,i}$ are respectively the refractive volume and the number density of the i-th constituent. Unlike the effect of ionosphere, the contribution of neutral gases to the refractivity is independent of frequency. Values of k_i can be determined experimentally and are known for the most abundant species in planetary atmospheres [17]. If the composition of the atmosphere is known, Equation 1.5 can be written as:

$$\nu_n = k n_n \tag{1.6}$$

where k is the mean refractive volume and n_n the total neutral number density. By means of Equation 1.6, the neutral number density as a function of altitude, $n_n(R)$, can be estimated from $\nu_n(R)$. The density profile can then be derived multiplying the neutral number density profile by the mean molecular mass m of that atmosphere:

$$\rho(r) = mn_n(r) \tag{1.7}$$

Using models of the gravitational field and possible non-gravitational accelerations, such as centrifugal accelerations due to the presence of winds, the pressure profile $p(R)$ can be inferred solving for hydrostatic equilibrium. Finally, the temperature profile $T(R)$ is obtained from $p(R)$ and $\rho(R)$ using an equation of state.

In principle, the two components of refractivity ν_e and ν_n cannot be distinguished using a single measurement. However, some assumptions on the atmospheric structure allow for the separation of these effects. Neutral gases typically experience an exponential decay of density with increasing altitude, while ionospheres are usually characterized by density peaks at high altitudes, and extremely low densities below the peak, as shown in Figure 1.2. As the two refractivities have opposite signs and opposite trends with respect to altitude, a vertical separation of the effect is possible: the measured ν can be fully attributed to either ν_e (if $\nu < 0$) or ν_n (if $\nu > 0$), assuming the other is negligible in the given region. The two effects can also be isolated performing simultaneous experiments at multiple frequencies, as ν_e is frequency dependent, in contrast to ν_n [17].

As radio occultations strongly rely on frequency measurements, it is desirable that the transmitted radio signals are generated using a sufficiently stable reference oscillator, capable of maintaining an almost constant frequency throughout the experiment. The stability of an oscillator is described by the Allan Deviation σ_{AD}, defined as:

$$\sigma_{AD} = \frac{1}{2}\langle(y_{n+1} - y_n)^2\rangle \tag{1.8}$$

where angle brackets denote the expectation value and the quantity y_n is related to the n-th sample period. y is defined as:

$$y = \frac{f_{meas} - f_{nom}}{f_{nom}} \tag{1.9}$$

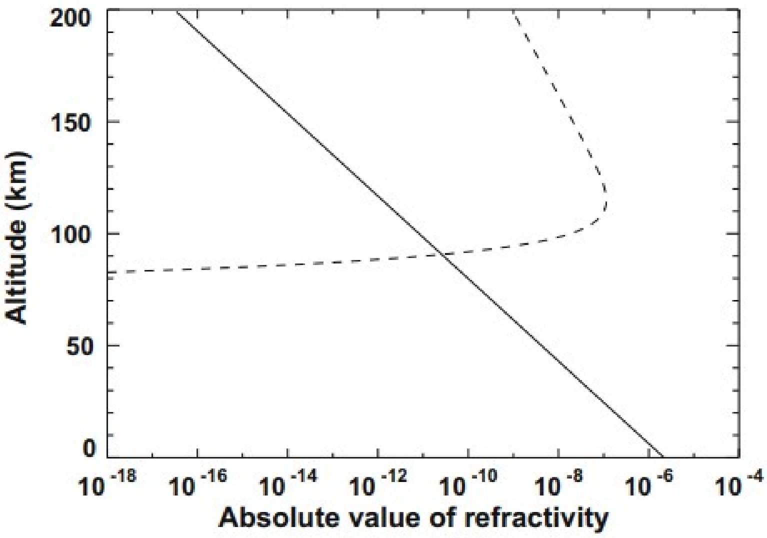

Figure 1.2: ν_n (solid line) and $-\nu_e$ (dashed line) in an ideal atmosphere [17].

where f_{meas} is the frequency computed in the correspondent sample period and f_{nom} the nominal frequency. σ_{AD} is a function of the sample period, or integration time, τ, over which the signal is integrated to estimate the frequency. Values of Allan Deviation for on-board oscillators able to perform radio occultations range in the order of 10^{-13}: if the spacecraft carries an oscillator that satisfies this requirement, radio occultations can be performed in a one-way fashion, which means using a single downlink monotone radio signal, transmitted by the spacecraft and received by a ground station. Conversely, if the on-board oscillator is not accurate enough, a reference uplink signal generated by a ground oscillator is needed, resulting in a two-way occultation architecture [17].

1.3 The Cassini mission

Cassini-Huygens was a space mission developed by NASA, ESA, and the Italian Space Agency (ASI) with the objective of studying the planetary system of Saturn. The mission included a main orbiter, Cassini, and the probe Huygens, designed to land on the surface of

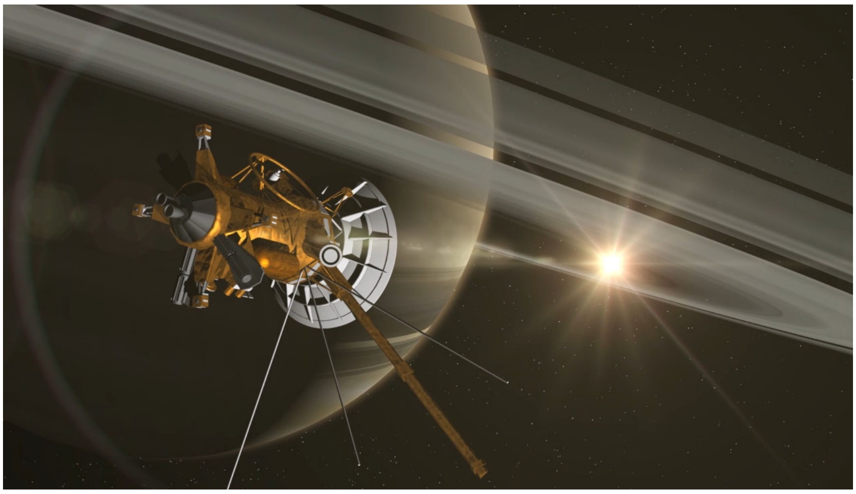

Figure 1.3: Representation of Cassini before the Mission Finale. Credits: NASA/JPL.

Saturn's moon Titan. Launched from Cape Canaveral on October 15, 1997, Cassini entered the orbit of Saturn on June 30, 2004, after a seven-year journey which included multiple gravity assists from Venus, the Earth, and Jupiter. Huygens successfully landed on Titan on January 14, 2005, becoming the first probe to ever reach the surface of a celestial body in the outer Solar System. The primary mission for the orbiter Cassini was a four-year exploration of the Saturn system, initially set to conclude in 2008. However, the mission was extended twice, eventually concluding on September 15, 2017, when the spacecraft was directed into Saturn's atmosphere to protect the moons of the gas giant from possible contamination and to collect additional scientific data. Cassini is widely considered as one of the most successful space missions in history due to its nearly 20-year lifespan. The probe orbited Saturn for 13 years, collecting precious experimental data, resulting in significant discoveries concerning the planet, its satellites, and its ring system. Some of the most important findings of Cassini are related to the moons of Saturn, for which little information was available before the arrival of the spacecraft. The numerous fly-bys of Titan revealed the presence of liquid methane flowing on its surface, as well as the existence of large masses of subsurface liquid water and ammonia. Observations of Enceladus detected the presence of intense

Band	Frequency (MHz)	Wavelength (cm)
S-band	2298	13
X-band	8425	3.6
Ka-band	32028	0.9

Table 1.1: Cassini downlink frequencies and bands used for radio science [2].

water vapor jets which interact with the ring system of Saturn [1]. The discovery of water on the two moons attracted the attention of the scientific community, as water is a fundamental component for life: this finding was a determinant factor in the decision to dispose of the spacecraft with its destruction into the atmosphere of Saturn.

In order to analyze the Saturn system, Cassini carried 12 scientific payloads, including optical remote sensing instruments ranging from infrared to ultraviolet electromagnetic radiation, as well as devices to measure the electromagnetic field and the properties of plasma and dust particles. Radio science experiments, including radio occultations, were performed by the RSS (Radio Science Subsystem), which exploited the High Gain Antenna (HGA) provided by ASI to transmit radio signals at three different frequencies, in S-, X-, and Ka- bands. The frequencies used for radio science are reported in Table 1.1. All signals were received on the Earth by the DSN stations, located in Goldstone, California; Canberra, Australia; and Madrid, Spain. The geographical position of these facilities allows for a continuous visibility of the Earth for all deep space probes. Signals used for radio science were generated using as a reference clock the Ultra-Stable Oscillator (USO), a quartz crystal oscillator produced by Johns Hopkins University, characterized by Allan Deviations in the order of 10^{-13} for integration times from 1 to 1000 seconds. The high stability of the USO allowed for the proper execution of one-way occultations until its failure in 2011, after which these experiments continued to be conducted in a two-way mode [2].

Radio occultations were successfully performed on the atmospheres of

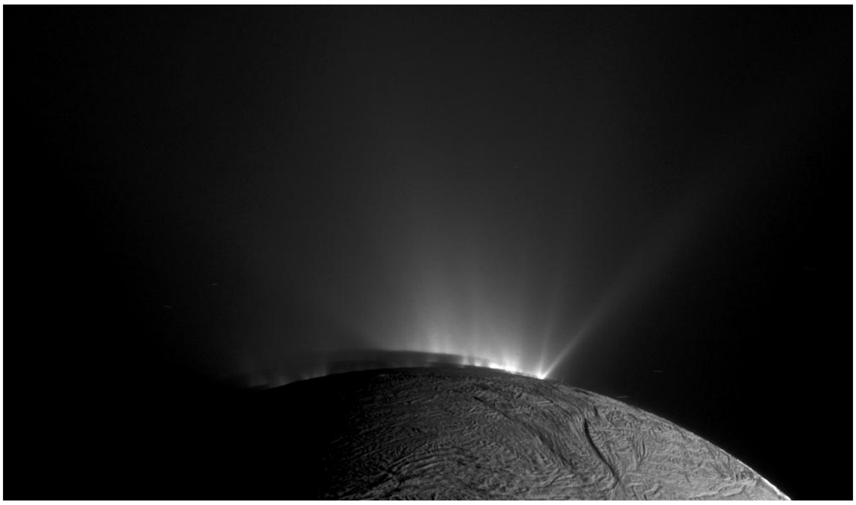

Figure 1.4: Enceladus water jets observed by Cassini. Credits: NASA/JPL-Caltech/Space Science Institute.

Saturn and Titan, allowing for the reconstruction of vertical profiles of pressure and temperatures, as well as on the rings of Saturn.

1.4 Enceladus

Enceladus is a moon of Saturn, discovered in 1789 by the astronomer William Herschel. It was first explored by Voyager 1 and Voyager 2, which passed by the celestial body respectively in 1980 and 1981, collecting high-resolution images of its surface. These earliest close inspections of Enceladus revealed a large variety of superficial features despite the small dimensions of the satellite (the diameter of Enceladus is 504 km): the alternation of cratered regions and smooth, younger terrains suggested the presence of ongoing geological activity [14].
After the passing of the Voyager probes, the satellite remained unexplored until the arrival of Cassini in the Saturn environment. Enceladus was one of the main targets of the mission, with a total of 23 fly-bys performed from 2005 to 2015. Geological activity on Enceladus was directly observed for the first time when pictures taken by Cassini evidenced the existence of intense plumes composed of water vapor and icy particles, located in the South Polar region of the moon. Most of the observed jets spout from elongated fissures, commonly re-

ferred to as "tiger stripes". Velocities reached inside Enceladus plumes are high enough to permit some particles to escape the gravitational field of the satellite and feed the E ring of Saturn, which would otherwise be unstable. The presence of water jets revealed the existence of an internal ocean of water, as well as a source of internal heat, which could be explained by dissipations related to tidal forces, caused by the eccentric orbit of Enceladus and by its resonance with the orbit of the Saturn moon Dione [10]. The continuous emission of material from the internal ocean of Enceladus is responsible for the presence of high density plasma surrounding the icy moon and extending for tens of Enceladus radii. This plasma environment is commonly referred to as "dusty plasma" due to the coexistence of ice particles, ions, and electrons, which strongly interact with each other [7]. Measurements for electron and ion densities in the dusty plasma environment were collected by the Radio and Plasma Wave Science (RPWS) instrument on-board Cassini and are discussed in subsection 5.3.1. Recent analysis of Cassini's Cosmic Dust Analyzer mass spectra of ice grains around Enceladus reveal the presence of sodium phosphates in these particles, suggesting the existence of phosphorus in the internal ocean of the moon [11]. This discovery represents the first detection of this element, fundamental for life, in an extraterrestrial ocean. Radio science capabilities of Cassini were employed to perform two radio occultations of Enceladus, including one which covered the geologically active regions of the satellite. The next chapters of this document describe the methodology applied to data from occultations of Enceladus and the obtained results.

Chapter 2

Occultations of Enceladus

Two radio occultations of Enceladus were conducted during the Cassini mission, with the first occurring on September 15, 2006. Although the initial plan was a grazing occultation, in which signals would have passed close to the surface of the celestial body without interacting with it, the actual result was different: electromagnetic rays hit the satellite, resulting in a one-minute loss of signal observed by the ground station during the experiment. The second occultation of Enceladus happened on January 26, 2010: this time, electromagnetic waves trasmitted by Cassini were successfully observed at ground station antennas without interruptions, indicating that a grazing occultation had been successfully achieved.

2.1 2010 occultation

2.1.1 Geometry and timeline

On January 26, 2010, Cassini performed radio occultation experiments in the vicinity of Enceladus: monotone radio signals in S-, X-, and Ka-bands, generated using the USO as a reference clock, were sent to the Earth. The transmission by Cassini started at 14:23 UTC, spacecraft time, and lasted for about one hour and a half: signals sent from 14:37 to 15:54 passed by the moon at distances smaller than 30,000 km from its center. The minimum distance was achieved by the ray emitted at 15:13:29, which passed over the surface of Enceladus at an altitude of 52 km, equivalent to a distance of 304 km from the moon's center. The first signals reached the Earth at 15:36 UTC after traveling for around 1.25 hours at the speed of light and were received at the Canberra Deep Space Communication Complex: here, the DSS-43 antenna, characterized by a diameter of 70 m, collected signals in S- and X-bands, while DSS-34, a 34-m antenna, measured waves in both X- and Ka-bands. Since signals were received continuously throughout the experiment, this occultation is commonly referred to as "grazing" in contrast to traditional occultations, in which signals are indeed "occulted" by the presence of the celestial body on the line of sight of the Earth from the spacecraft. After the observation of Enceladus, Cassini continued performing occultations for some hours, analyzing the rings and the atmosphere of Saturn.

The geometry of all the bodies involved in the radio occultation experiment can be reconstructed using SPICE routines, developed by NASA's Navigation and Ancillary Information Facility (NAIF) to manage ephemeris data, widely used for space applications, including spacecraft navigation and data analysis. The information related to positions and velocities of spacecrafts and celestial bodies at a given time is stored in SPK files: for our analysis, the ephemeris of Enceladus, Cassini, and the Earth are necessary to calculate the trajectory of the electromagnetic rays transmitted by Cassini and the minimum distance from the moon's center reached as a function of time. The geometry of the occultation is depicted in Figure 2.1. Electromagnetic waves transmitted by Cassini propagated towards the Earth, moving approximately on the equatorial plane of Saturn, and approaching Enceladus. As the picture suggests, the grazing occultation occurred in the South Polar region of Enceladus, at latitudes as high as 85°S: as the cryovolcanic activity of the moon is expected to happen in this region, the occultation in question appears to be suitable to analyze these phenomena.

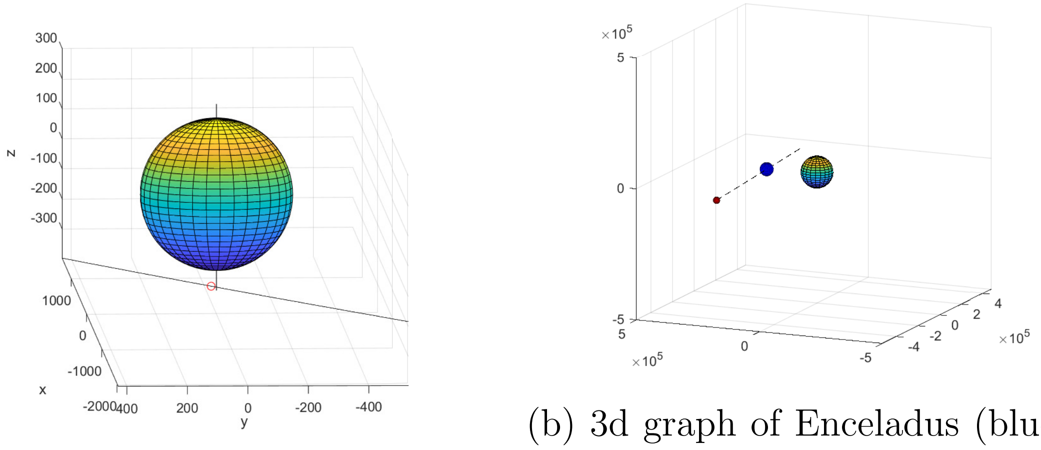

(a) Points of closest approach of the signal to Enceladus.

(b) 3d graph of Enceladus (blue), Cassini (red), Saturn (center), and Cassini-Earth line (dashed).

Figure 2.1: 3d representation of the occultation of January 26, 2010.

2.1.2 Radio signals

Radio signals have been recorded by Radio Science Receivers (RSRs), open-loop receivers which convert electromagnetic waves from analogic to digital form, allowing for an accurate preserving of information [2]. Raw files produced by RSRs are stored at the NASA Planetary Data System (PDS) and are accessible by the scientific community to reconstruct the original signals. Since our analysis relies on received frequencies, signals have been recovered as time series of frequencies. This form of representation requires the division of the whole data set in equally spaced time intervals, over which a Fourier transform is performed to determine the frequency at which the power spectrum is maximized: this value is then assigned to the middle point of that interval [4]. The integration time τ, equal to the length of each time interval, is a design parameter for this operation: a small value of τ is desirable for a better space resolution, as it would result in a larger number of data points. However, reducing τ also increases the sensitivity of measurements to noise. For our analysis, τ has been set to 1 s, a value consistent with other radio occultation studies.

Starting from the archived RSR raw data, time sequences of frequencies have been reconstructed for the following signals received during the 2010 occultation:

- S-band signal received by DSS-43;
- X-band signal received by DSS-43;
- X-band signal received by DSS-34;
- Ka-band signal received by DSS-34.

Each signal has been collected by two subchannels of the RSRs, which used two different sampling rates, equal to 1 kHz and 16 kHz. All time sequences of frequencies, reported in Figure 2.2, experience an almost linear increasing trend, mainly caused by Doppler effect, with a difference between the first and the last measurement of $1.8 \cdot 10^{-6}$ times the frequency value at the first instant of time. The offset between the measurements obtained using the two sampling rates, shown in Figure 2.3, maintains smaller than 0.5 mHz for the S-band signal, while for the other bands this quantity experiences higher values, up to 0.6 mHz for the X-band signals and 2 mHz in Ka-band. The magnitude of this feature has to be compared to the results of further analyses, reported in the next sections, to determine whether or not the sample rate selection is determinant for this analysis. The signal to noise power ratios C/N_0 for the received signals are reported in Figure 2.4. Recordings collected at a sample rate of 16 kHz better perform in terms of this parameter. For this reason, these sets of data appear to be more suitable for the following analyses. It is worth noting the reduction of C/N_0 of the X-band signal when received by the DSS-34, consistently with the smaller diameter of that antenna, as well as a higher variability of this property for the Ka-band signal, more susceptible to weather effects due to its shorter wavelength.

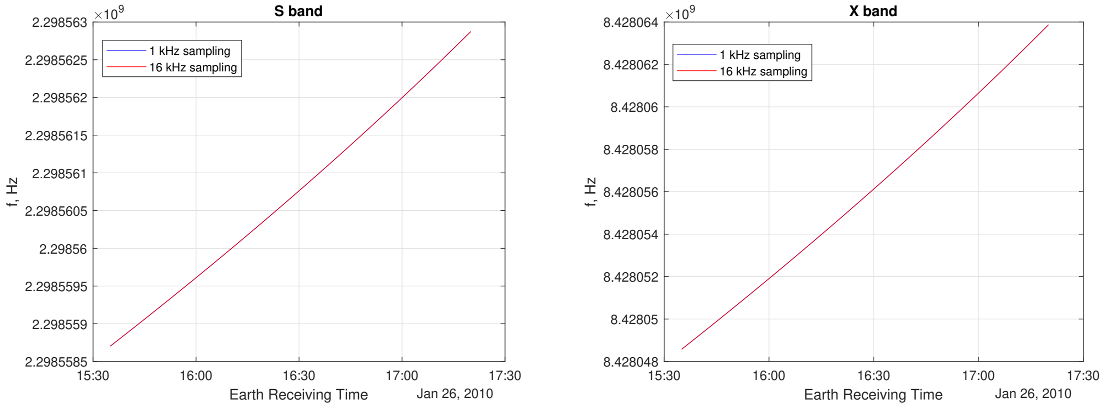

(a) S-band (DSS-43). (b) X-band (DSS-43).

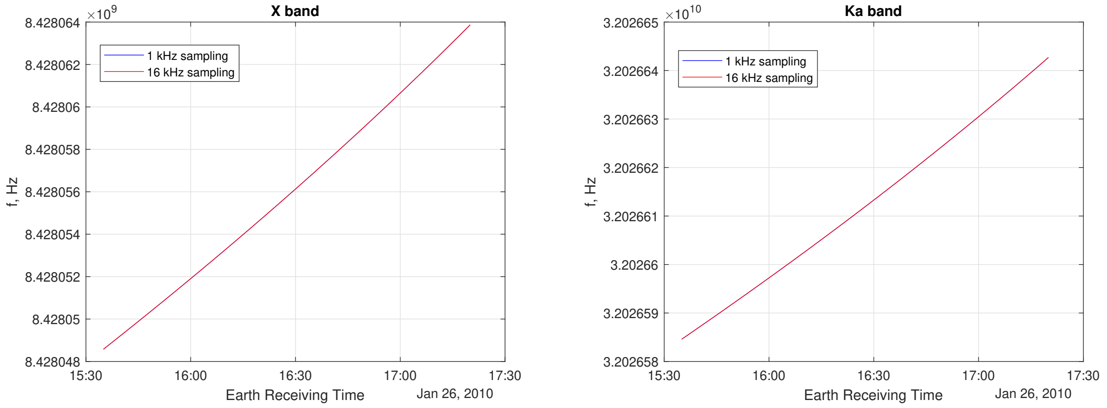

(c) X-band (DSS-34). (d) Ka-band (DSS-34).

Figure 2.2: Received frequency data for the Enceladus occultation of January 26, 2010.

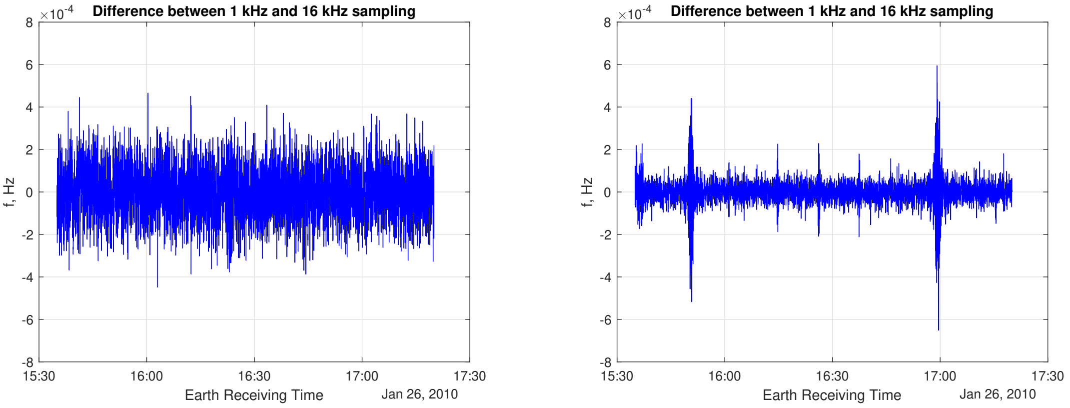

(a) S-band (DSS-43).

(b) X-band (DSS-43).

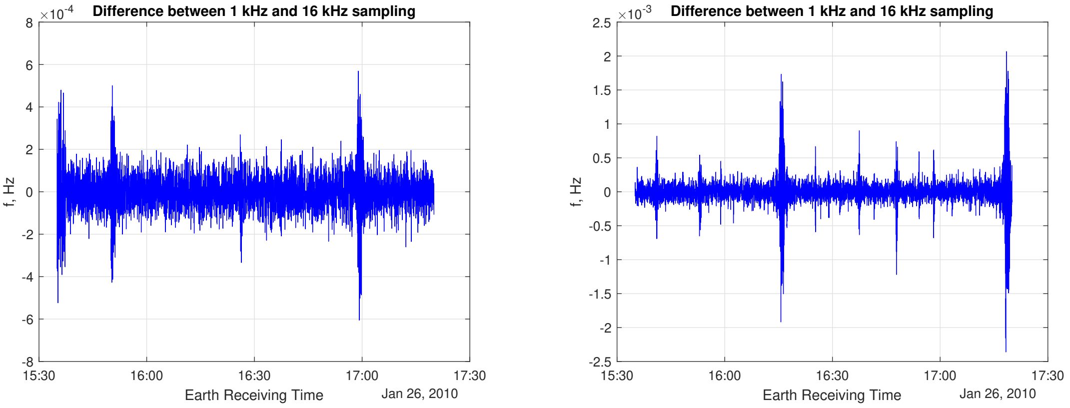

(c) X-band (DSS-34).

(d) Ka-band (DSS-34).

Figure 2.3: Difference between frequency data sampled at 16 kHz and 1 kHz, occultation of January 26, 2010.

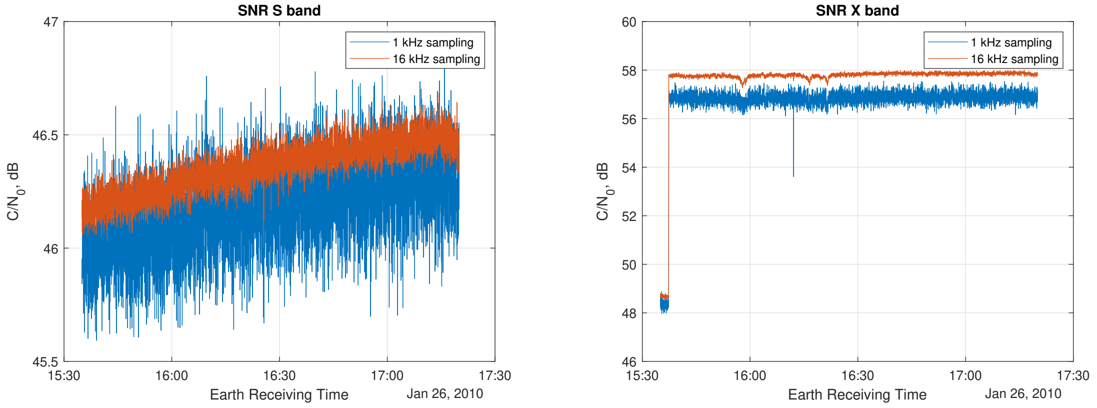

(a) S-band (DSS-43).

(b) X-band (DSS-43).

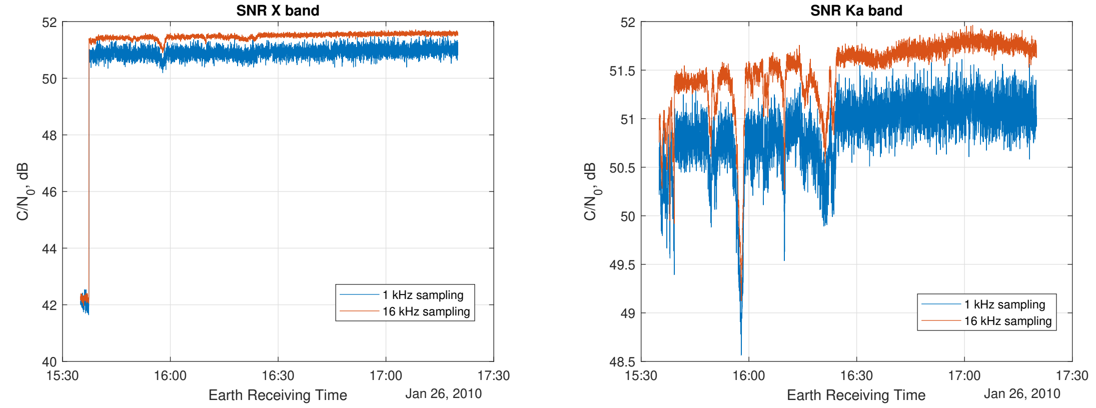

(c) X-band (DSS-34).

(d) Ka-band (DSS-34).

Figure 2.4: Signal to noise power ratios of the Enceladus occultation of January 26, 2010.

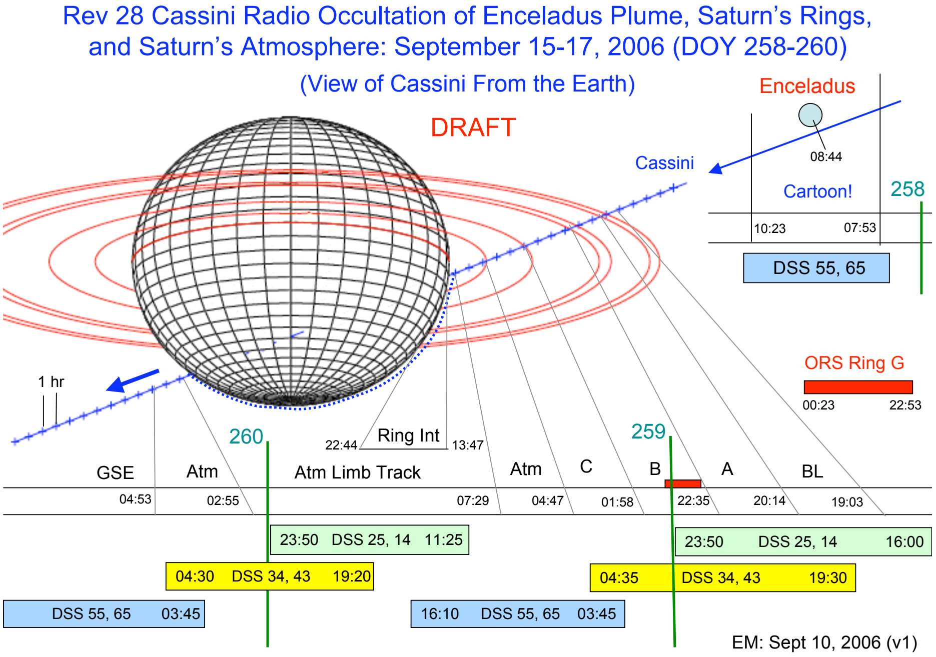

Figure 2.5: Draft representation of the radio occultations performed by Cassini on September 15-17, 2006 [16].

2.2 2006 occultation

2.2.1 Geometry and timeline

The first radio occultation of Enceladus occurred on September 15, 2006, when Cassini emitted radio signals in three bands towards the Earth direction, starting at 6:30 UTC, spacecraft time, and continuing until 9:00. Signals were collected on the Earth from 7:50 UTC onward at the Madrid Deep Space Communications Complex, where two 34-m antennas were tracking: DSS-65 measured signals in S- and X-bands, while DSS-55 collected those in X- and Ka-bands. A draft picture of the occultation in question present in the Planetary Data Science archive [16], reported in Figure 2.5, suggests that a grazing occultation was scheduled, similar to the one that occurred in 2010. However, when the experiment was performed, the real outcome was a traditional occultation, in which signals reached the surface of Ence-

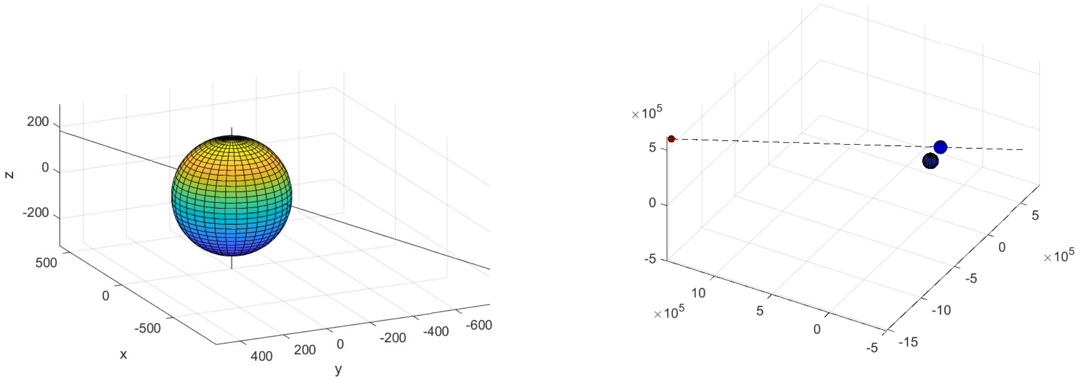

(a) Points of closest approach of the signal to Enceladus.

(b) 3d graph of Enceladus (blue), Cassini (red), Saturn (center), and Cassini-Earth line (dashed).

Figure 2.6: 3d representation of the occultation of September 15, 2006.

ladus in a small window of time, instead of remaining above a certain altitude, as testified by the interruption of the incoming signal at the DSN antennas. In the days following the Enceladus occultation, Cassini proceeded with radio science experiments on the Saturn rings and on the upper atmosphere of the gas giant.

A reconstruction of the geometry of the occultation, reported in Figure 2.6, has been obtained utilizing SPICE routines. This analysis confirmed that electromagnetic waves emitted by Cassini from 7:20:32 to 7:21:21 UTC struck the Enceladus surface: this window of time is consistent with the one related to the absence of received signal at the Deep Space Network antennas. The occultation happened in the equatorial regions of the moon, as the ingress scanned locations at latitudes between the equator and 5°S, whereas the egress covered latitudes between 15° and 20°N. This time, the path of electromagnetic rays propagating in the direction of the Earth was inclined with respect to the equatorial plane of Saturn. Although the geometry of the 2006 occultation did not involve Enceladus plumes, the same analysis has been conducted for completeness.

2.2.2 Radio signals

Time sequences of frequencies have been produced from the RSR raw data, using an integration time τ of 1 s, for the following signals measured by the Deep Space Network antennas at the Madrid Deep Space Communications Complex during the radio occultation of 2006:

- S-band signal, received by DSS-65;
- X-band signal, received by DSS-65;
- X-band signal, received by DSS-55;
- Ka-band signal, received by DSS-55.

The above-mentioned frequency measurements are shown in Figure 2.7. In the time window from 8:43:34 to 8:44:23, UTC, all the antennas measured noise in the correspondent bands due to the absence of Cassini signals, occulted by the surface of Enceladus. A decreasing trend is noticeable in all frequency measurements, with a total difference in frequency values equal to $3.3 \cdot 10^{-7}$ times the first measured value. The frequency differences between the sequences obtained from sampling rates of 1 kHz or 16 kHz are reported in Figure 2.8: X-band signals are characterized by maximum offsets of around 0.3 mHz, whereas the difference in the measurements in S- and Ka-band reaches values higher than 1 mHz. The relevance of the sampling time selection on the outcomes is assessed in section 4.2, where analysis of frequency data reported here is performed. The signal to noise power ratio C/N_0 is shown in Figure 2.9. Similarly to the 2010 occultation, data digitalized at 16 kHz is characterized by better values of C/N_0, therefore seeming more suitable for subsequent analyses. With respect to that occultation, the C/N_0 of the received S-band signal is considerably lower, since it has been collected by a smaller antenna. For the other measurements, values of signal to noise power ratio are comparable to those of the 2010 occultation received by the 34-m antenna. Moreover, the Ka-band signals experiences similar variabilities in this quantity.

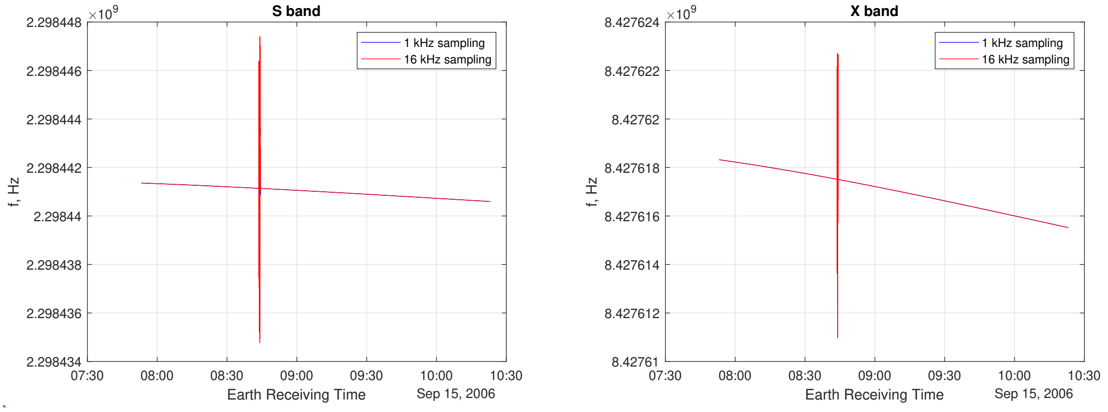

(a) S-band (DSS-65).

(b) X-band (DSS-65).

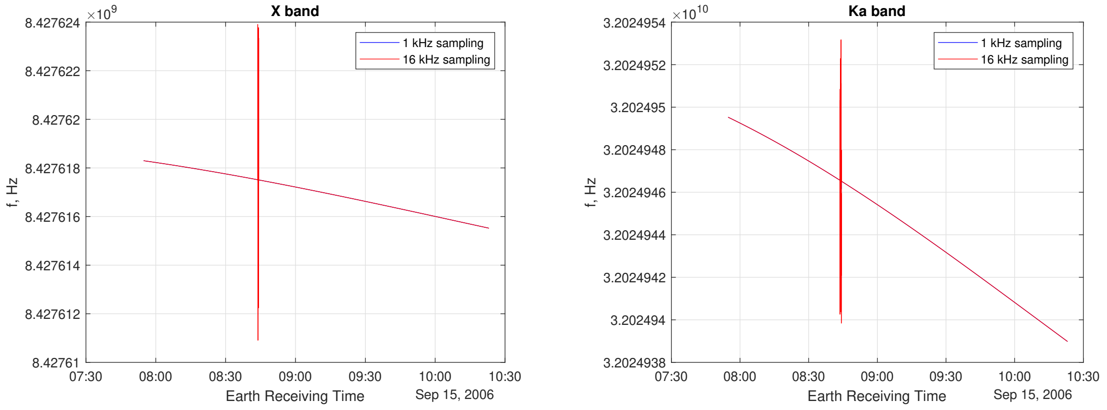

(c) X-band (DSS-55).

(d) Ka-band (DSS-55).

Figure 2.7: Received frequency data for the Enceladus occultation of September 15, 2006.

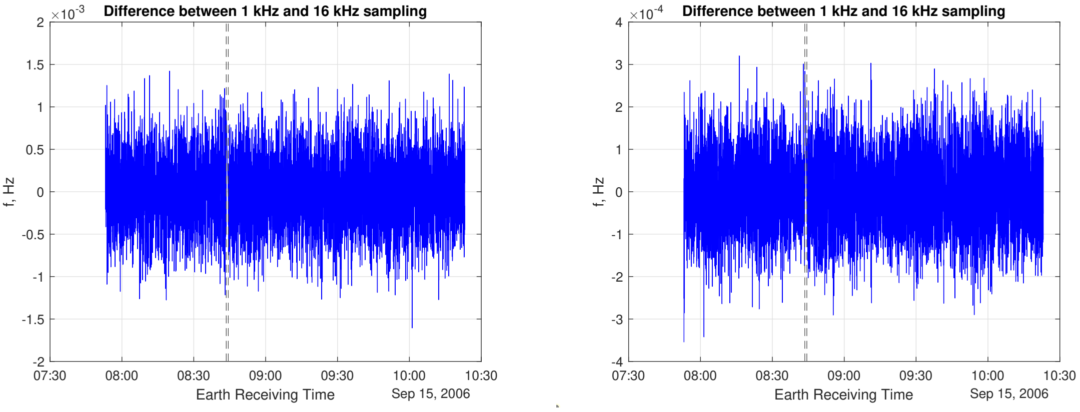

(a) S-band (DSS-65). (b) X-band (DSS-65).

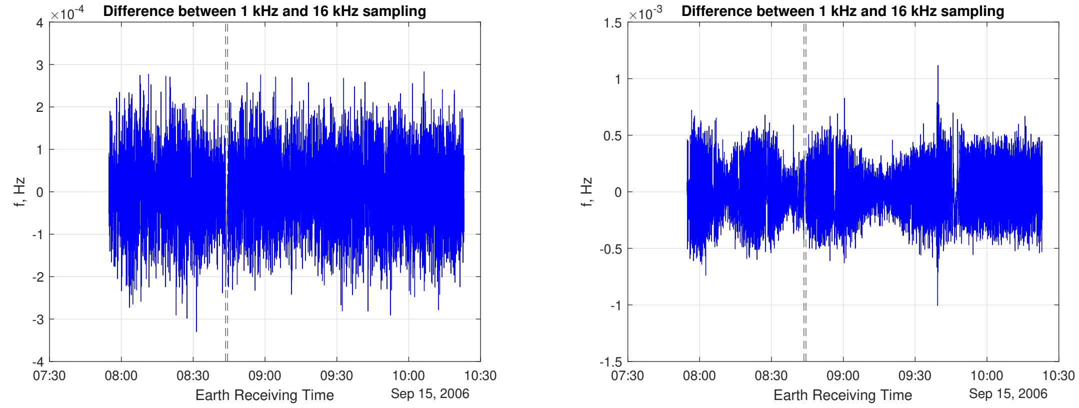

(c) X-band (DSS-55). (d) Ka-band (DSS-55).

Figure 2.8: Difference between frequency data sampled at 16 kHz and 1 kHz, occultation of September 15, 2006.

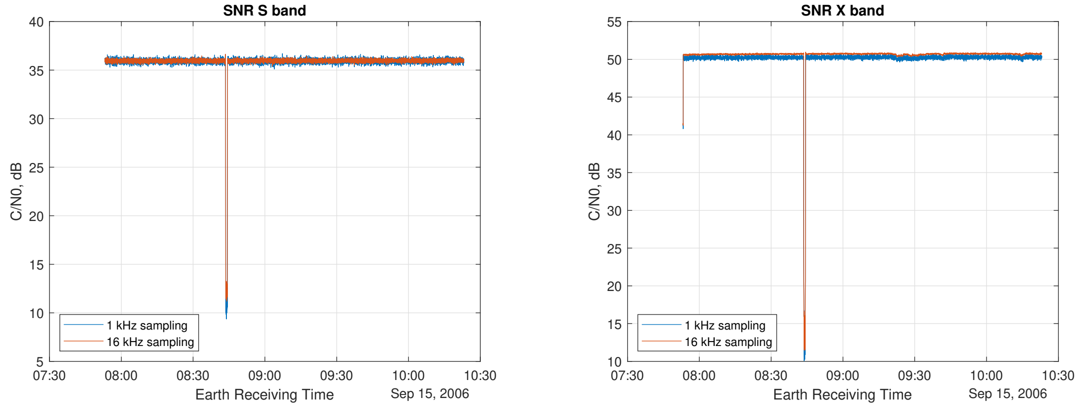

(a) S-band (DSS-65).

(b) X-band (DSS-65).

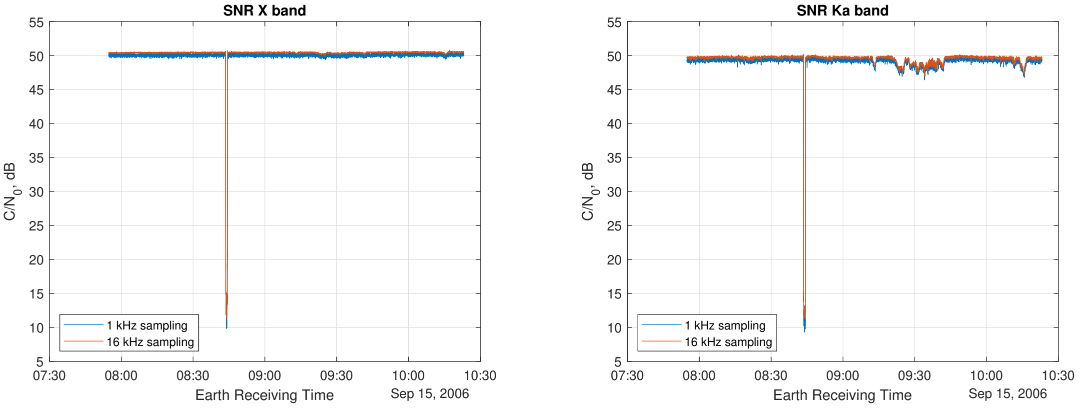

(c) X-band (DSS-55).

(d) Ka-band (DSS-55).

Figure 2.9: Signal to noise power ratios of the Enceladus occultation of September 15, 2006.

Chapter 3

Methodology

As the radio occultations in question were performed in multiple bands and in a one-way geometry, electron density measurements can be inferred using two independent signals at different frequencies, combined to isolate that effect.

3.1 Total electron content

The relationship between the frequency of an electromagnetic wave when received at a ground station antenna with respect to the frequency transmitted by the spacecraft, reported in Equation 1.2, can be recast, using the expressions of ν_e and ν_n in Equations 1.4 and 1.6, and neglecting relativistic effects, as:

$$f_R = f_T - \frac{f_T}{c}\frac{d}{dt}\int dl + \frac{e^2}{8\pi^2 m_e \varepsilon_0 c f_T}\frac{d}{dt}\int N_e dl - \frac{f_T k}{c}\frac{d}{dt}\int n dl \qquad (3.1)$$

where dl is the infinitesimal path length. The transmitted frequency f_T is affected by three contributions, which are respectively the Doppler effect, the effect of electrons crossed by the ray, and the effect of neutral particles encountered on the path. During occultations, the three downlink monotone signals were transmitted using the same reference source, which was the on-board USO: as a result, these signals were coherent, and their frequencies respected precise ratios at transmission, reported in Table 3.1. Although these relationships between frequen-

Band couple	Frequency ratio
S-band/X-band	3/11
X-band/Ka-band	5/19

Table 3.1: Ratios between Cassini downlink frequencies used for radio science.

cies are not valid at reception, due to the frequency dependence of Equation 3.1, their validity at transmission allows for the development of a simple methodology for the analysis of the occultations in question. Using Equation 3.1 for two specific frequency bands, such as S- and X-bands:

$$\begin{aligned} f_{R,S} &= f_{T,S} - \frac{f_{T,S}}{c}\frac{d}{dt}\int dl + \frac{e^2}{8\pi^2 m_e \varepsilon_0 c f_{T,S}}\frac{d}{dt}\int N_e dl - \frac{f_{T,S}k}{c}\frac{d}{dt}\int n dl \\ f_{R,X} &= f_{T,X} - \frac{f_{T,X}}{c}\frac{d}{dt}\int dl + \frac{e^2}{8\pi^2 m_e \varepsilon_0 c f_{T,X}}\frac{d}{dt}\int N_e dl - \frac{f_{T,X}k}{c}\frac{d}{dt}\int n dl \end{aligned} \tag{3.2}$$

Combining the two equations and using the relationship between the transmitted frequencies $f_{T,S} = \frac{3}{11} f_{T,X}$, the Doppler shift and the effect of neutral atmosphere can be removed, highlighting the effect of plasma:

$$f_{R,S} - \frac{3}{11} f_{R,X} = \frac{e^2}{8\pi^2 m_e \varepsilon_0 c f_{T,S}} \left(1 - \left(\frac{3}{11}\right)^2\right) \frac{d}{dt}\int N_e dl \tag{3.3}$$

Analogously, using the couple formed by X- and Ka-bands and the relationship $f_{T,X} = \frac{5}{19} f_{T,Ka}$, the result is:

$$f_{R,X} - \frac{5}{19} f_{R,Ka} = \frac{e^2}{8\pi^2 m_e \varepsilon_0 c f_{T,X}} \left(1 - \left(\frac{5}{19}\right)^2\right) \frac{d}{dt}\int N_e dl \tag{3.4}$$

Finally, denoting as Δf the left-hand side of the equations above and rearranging:

$$\frac{d}{dt}\int N_e dl = \Delta f_{SX} \frac{8\pi^2 m_e \varepsilon_0 c f_{T,S}}{e^2} \frac{1}{1 - \left(\frac{3}{11}\right)^2} \tag{3.5}$$

$$\frac{d}{dt}\int N_e dl \; = \Delta f_{XK}\frac{8\pi^2 m_e \varepsilon_0 c f_{T,X}}{e^2}\frac{1}{1-\left(\frac{5}{19}\right)^2} \tag{3.6}$$

The quantity $\int N_e dl$ is commonly referred to as total electron content (TEC, or in some works Ω), and represents the number of electrons encountered by an electromagnetic ray, integrated along its path. As N_e is the number of particles per unit volume (m^{-3}), the unit of measure of total electron content is m^{-2}. Using Equations 3.5 and 3.6, the temporal derivative of the total electron content can be estimated from time sequences of frequencies in two different bands: integrating by time this result, the TEC profile over time (apart from an integration constant) can be reconstructed [4]. In most applications, the equations above are preceded by a correction on the values of Δf to account for undesired effects affecting frequency measurements: these factors include variations in solar winds, system noise, effects of terrestrial atmospheres, and interplanetary plasma. Typically, the correction involves subtracting a linear fit of Δf calculated in a time interval, known as baseline, in which it is assumed that the electromagnetic waves transmitted by the spacecraft did not interact with the occulting body.

3.2 Electron Content via Abel Transform

Once a total electron content estimation over the occultation time is available, reconstructing vertical profiles of electron density requires some assumptions on the atmospheric properties. When analyzing small satellites, the hypothesis of spherical symmetry of the refractive environment usually yields acceptable results. If densities are spherically symmetric, the total electron content Ω is related to the electron density N_e as follows:

$$\Omega(X) = 2\int_{r=X}^{r=\infty} \frac{N_e dr}{\sqrt{r^2 - X^2}} \tag{3.7}$$

where X is the impact parameter, which is the distance from the occulting body of each ray at its point of closest approach, and r the radial distance from the center of the celestial body in question. Equation 3.7 can be inverted through an Abel transform to obtain a vertical profile of N_e:

$$N_e(r) = -\frac{1}{\pi}\int_{X=r}^{X=\infty} \frac{d\Omega(X)}{dX}\frac{dX}{\sqrt{X^2 - r^2}} \tag{3.8}$$

or, in an equivalent formulation [4]:

$$N_e(r) = \frac{1}{\pi}\int_{X=r}^{X=\infty} \ln\left(\frac{X}{r} + \sqrt{\left(\frac{X}{r}\right)^2 - 1}\right) d\left(\frac{d\Omega(X)}{dX}\right) \tag{3.9}$$

For our specific task, spherical symmetry may not be appropriate as the features to be observed are locally distributed. Since the water plumes are positioned in the vicinity of the South Pole and develop vertically, assuming a cylindrical symmetry could be more adequate for the analysis in question. Equation 3.9 can be reformulated for a cylindrically symmetric ionospheric environment by substituting radial distances with their respective axial counterparts:

$$N_e(\rho) = \frac{1}{\pi}\int_{X_a=\rho}^{X_a=\infty} \ln\left(\frac{X_a}{\rho} + \sqrt{\left(\frac{X_a}{\rho}\right)^2 - 1}\right) d\left(\frac{d\Omega(X_a)}{dX_a}\right) \tag{3.10}$$

where X_a is the distance of closest approach of each ray to the axis of rotation of Enceladus and ρ is the local distance from the axis of rotation.

The equations described above have been implemented in MATLAB environment. After computing the total electron content as a function of time $\Omega(t)$ using Equations 3.5 and 3.6, and determining the time sequence of distances of closest approaches $X(t)$ or $X_a(t)$ using SPICE routines, the algorithm proceeds as follows:

1. Total electron content is expressed as a function of distance of closest approach, $\Omega(X)$ or $\Omega(X_a)$;

2. The derivative of Ω with respect to X or X_a is calculated through difference of consecutive values;
3. The integrand function in Equation 3.10 is computed for each value of X or X_a;
4. For each ρ, the function is numerically integrated for values of distance of closest approach ranging from ρ to the last available value.

This routine requires splitting the measurements into two segments to properly perform the integration. In the case of the 2006 occultation, the division was straightforward, as the two segments were interrupted by the presence of the planet. For the 2010 grazing occultation, the observation was divided into an ingress and an egress at the time of minimum distance from the Enceladus center (or from its rotation axis for the cylindrically symmetric version).

Chapter 4

Results

This chapter illustrates the results of the analysis conducted on frequency data related to the occultations of Enceladus performed by Cassini, using the methodology described in chapter 3.

4.1 Results of 2010 occultation

Using the procedure outlined in section 3.1, the total electron content profiles for the January 26, 2010, occultation can be reconstructed from the time sequences of frequency differences Δf_{SX} and Δf_{XK}, reported in Figure 4.1. In each subfigure, the blue line represents the actual Δf of the respective band couple, calculated at each second as the difference between the smallest frequency and the highest one multiplied by the correspondent frequency ratio in Table 3.1, using frequency data collected at a sampling rate of 16 kHz. Values of Δf as a function of time have been averaged over a moving time window of 28 s for better visualization: the results of this operation are represented by the red lines. The behavior of Δf for the two band couples is similar, characterized by zero-mean oscillations within an absolute value of 7 mHz, with a few outliers. The standard deviations of the two results are comparable as well, being $\sigma_{f,SX}$ equal to 2.5 mHz and $\sigma_{f,XK}$ equal to 2.1 mHz. Frequency offsets between data obtained using a sampling time of 16 kHz or 1 kHz (Figure 2.3), when inserted in Equation 3.2 for the calculation of Δf, generate variations of this

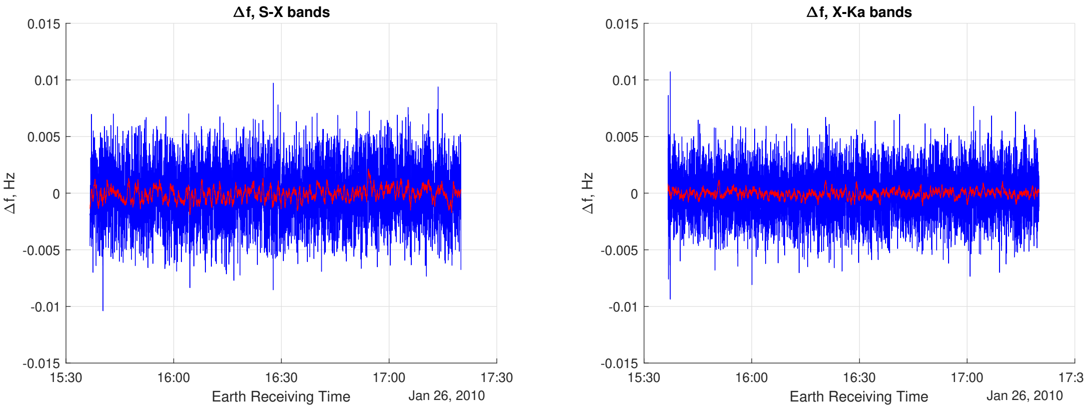

(a) S- and X-bands. (b) X- and Ka-bands.

Figure 4.1: Δf of the occultation of January 26, 2010.

quantity smaller than 0.6 mHz (although the frequency offset for the Ka-band can be as high as 2 mHz, this quantity is multiplied by 5/19 in Equation 3.2, resulting in a smaller value). As a result, the sampling rate selection does not significantly impact the outcome of this analysis. The time-averaged profiles show that short-term oscillations occur throughout the whole experiment with similar intensity, regardless of the distance of closest approach of the respective ray to Enceladus. No clear evidence of the crossing of atmospheric features is visible by just observing the time series of frequency differences. While some oscillations can be detected when the signals reached the minimum altitude over the moon surface (around 16:28, Earth Receiving Time), these are comparable to other variations that cannot be attributed to the vicinity to Enceladus.

By integration over time of Equations 3.5 and 3.6, the total electron content encountered by each ray at a given time can be estimated. Results shown in Figure 4.2 indicate the presence of a consistent descending trend over the entire duration of the experiment, with small oscillations occurring repeatedly. The time averaging of the Δf functions discussed earlier has the effect of smoothing the total electron content profiles obtained through integration, removing high-frequency variations without significantly affecting the overall behavior. Interestingly, the total variation in total electron content varies significantly between

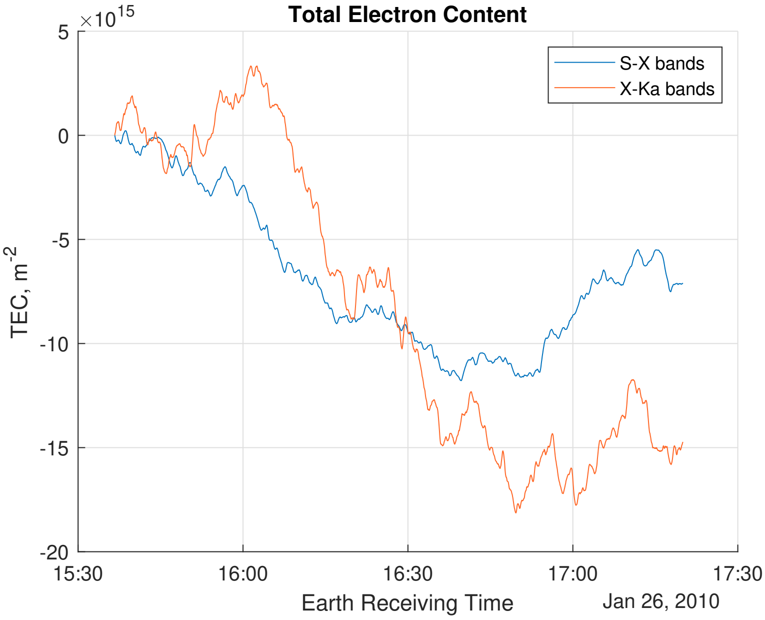

Figure 4.2: Total electron content before correction of Δf, 2010 occultation.

the results of the two couples. The difference between the maximum and minimum values obtained by analysis of S- and X-band signals is approximately $1 \cdot 10^{16}$ m^{-2}, whereas for the samples evaluated using X- and Ka-bands this quantity is almost double.

The results reported in Figure 4.2 have been obtained by directly utilizing the Δf values computed by frequency difference. When performing analysis of radio occultation data, it is common practice to correct these results, as frequencies are not only affected by the presence of the occulting body, but also by undesired effects which may cause the presence of bias in these measurements. In most applications, this operation is performed through the selection of a baseline positioned before or after the occultation, over which Δf is approximated through a polynomial fit. The obtained approximation is meant to represent the effects of interplanetary plasma and other sources of noise, which are challenging to predict and model, but are supposed to maintain relatively constant throughout the experiment. Usually, a linear fit performed over a time period when radio signals move at sufficient distance from the celestial body is sufficient to obtain sensible

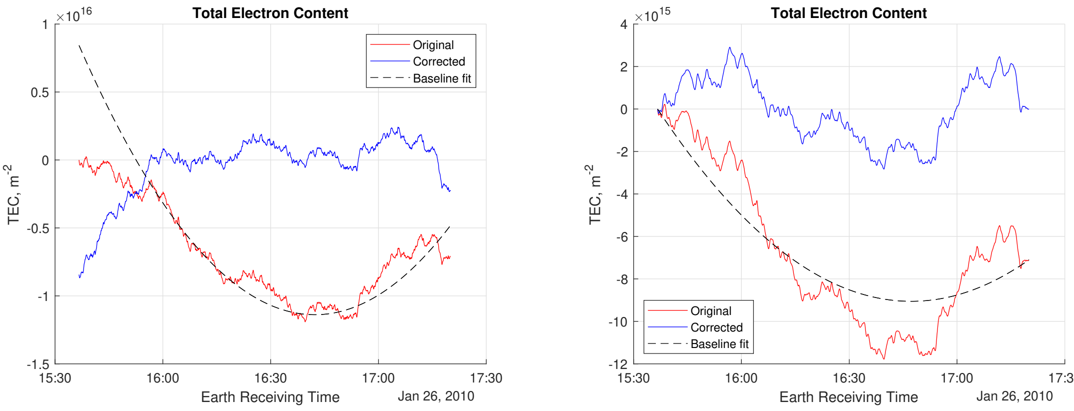

(a) General baseline, linear fit (usual approach).

(b) Linear fit over the whole time period.

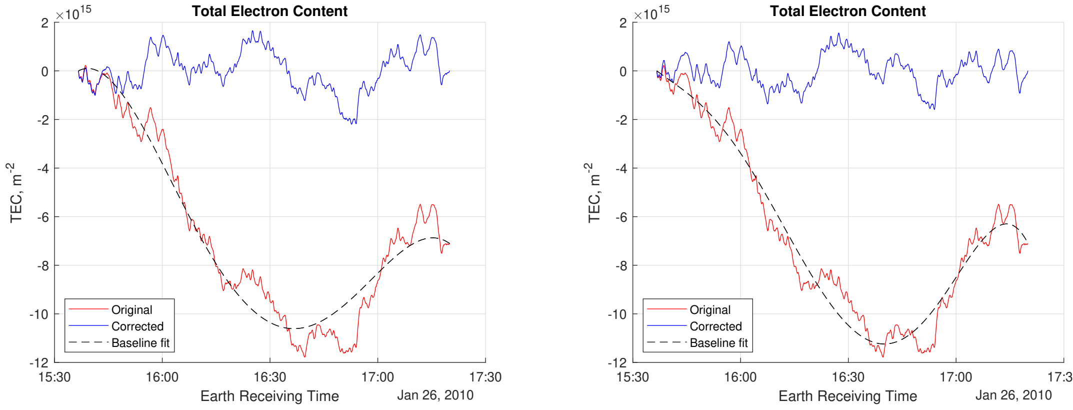

(c) 3rd-degree polynomial fit over the whole time period.

(d) 4th-degree polynomial fit over the whole time period.

Figure 4.3: Total electron content after some correction strategies for the 2010 occultation, obtained from S- and X-bands.

results. However, for the analysis in question, this strategy does not seem to provide appropriate outcomes. Multiple baselines, varying in length and covering different time intervals, either before or after the closest approach to Enceladus, have been tested. One of the results obtained with this procedure is shown in Figure 4.3a, where the red line represents the result of the direct integration without correction of Δf_{SX}, the blue line the corrected result, and the dashed line the difference between the two results. It is worth noting that the linear correction in the frequency domain yields a parabolic correction in total electron content, due to the integration with respect to time. The result in question is related to a linear fit performed defining as a baseline the time period between 15:58 and 16:10. Although the total electron content appears to oscillate around a constant value for most of the experiment time, the ascending trend at the beginning of the observation cannot be neglected. None of the tested corrections using this approach was able to produce a desirable outcome, which is a fairly constant total electron content over the whole duration of the experiment, with a peak in a reasonably wide area around the point of closest approach (16:28, Earth Receiving Time).

As the usual procedure did not properly function, a different strategy has been tested. The trend of the uncorrected total electron content, which is initially descending, and then ascending in the last portion of the observation, seems to indicate the presence of periodic variations in the plasma environment. The exploration of Saturn by the Voyager probes and by Cassini itself has proven the existence of periodicities in several features related to the magnetosphere of the planet, such as magnetic fields, radio emissions, and charged particles [3]. The involved varying quantities may affect, directly or indirectly, the results of a radio occultation: although these effects are usually not considered for the analysis of planetary atmospheres, they may be significant in the Enceladus environment, where smaller densities are expected. The periodic oscillations of the magnetospheric properties of Saturn are characterized by a period of approximately 10.7 hours, which is considered as the rotation period of the planet, while the observation

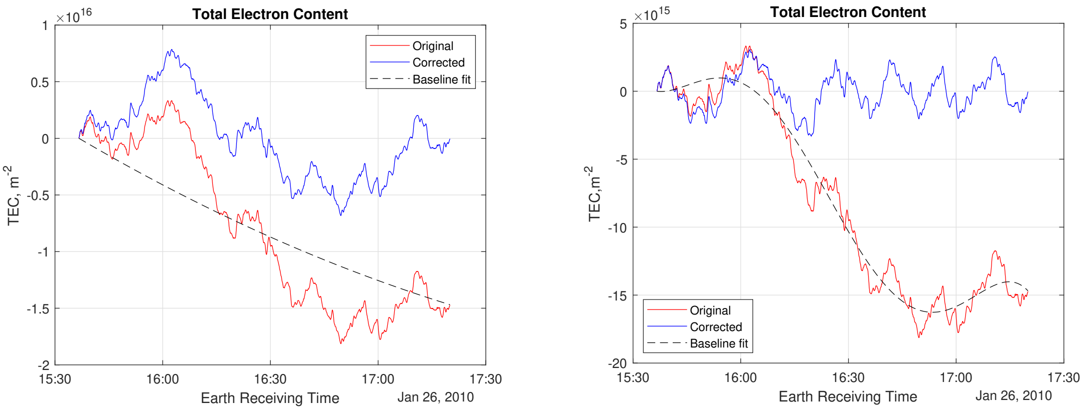

(a) Linear fit over the whole time period.

(b) 4th-degree polynomial fit over the whole time period.

Figure 4.4: Total electron content after some correction strategies for the 2010 occultation, obtained from X- and Ka-bands.

of Enceladus in question extended for roughly two hours, spanning a significant part of this period. This effect has been modeled with polynomial fits of various degrees over the entire duration of the experiment. The results of this procedure applied to the total electron content obtained from the Δf measurements related to the band couple S-X are shown in Figure 4.3. Figure 4.3b presents a linear correction, Figure 4.3c the 3rd-degree polynomial correction, and Figure 4.3d the 4th-degree polynomial correction. Polynomials of order higher than 4 were not considered suitable, as increasing the polynomial degree may generate artificial additional features that could invalidate measurements. Corrections with 3rd- and 4th-degree polynomial corrections highlight the presence of a peak lasting approximately 15 minutes around the time of minimum distance to Enceladus: this peak is characterized by total electron content variations of around $2 \cdot 10^{15}$ m^{-2}, a value which is still comparable to other oscillations occurring throughout the observation. A similar analysis has been conducted starting from Δf measurements related to the X- and Ka-band signals. Some of the results are reported in Figure 4.4: as for the outcome computed from the other band couple, correcting the total electron content by subtracting a 4th-degree polynomial fit can remove long-term variations of this quantity highlighting local oscillations. However, those occurring near the time of minimum distance to the moon are not more intense than the others. The same procedure can also be applied to total electron content estimations obtained through different procedures, such as a weighted average of TEC measurements derived by the two band couples, or using the third couple, formed by the S- and Ka-band signals. However, using different combinations of the same frequency data is not expected to provide additional information. Therefore, both of these alternative approaches would yield outcomes dependent on the results already presented.

Vertical profiles of electron density, produced using the methodology illustrated in section 3.2, are presented in Figure 4.5. Figures 4.5a and 4.5b show the estimated electron density derived from linear corrections of total electron content for the S-X and X-Ka bands (the corresponding TEC profiles are visible in Figures 4.3b and 4.4a), whereas Figures 4.5c and 4.5d illustrate the same quantity, obtained from the total electron content profiles corrected with 4^{th}-degree polynomials (profiles in Figures 4.3d and 4.4b). Electron content profiles have been calculated using both the spherical and the cylindrical versions of the Abel transform described in section 3.2: interestingly, no significant difference is noticeable between the results of the two strategies. All the results reported in this section refer to the cylindrical version of the Abel transform. For numerical stability of this method, a small number of samples had to be excluded from the computation: in particular, close to the minimum distance to Enceladus, the vertical step, which is the difference between the distance of closest approach of one sample and the previous one, becomes significantly smaller, while total electron content does not experience analogous variations. As a result, the term $d\left(\frac{d\Omega(X_a)}{dX_a}\right)$ grows indefinitely, causing divergence of the electron density to either positive or negative values. Solving this issue required sacrificing the samples collected in a 10-second time window around the time of minimum distance to Enceladus. Intense oscillations are visible for all altitudes, indicating the presence of high uncertainties in these measurements. When using the reported

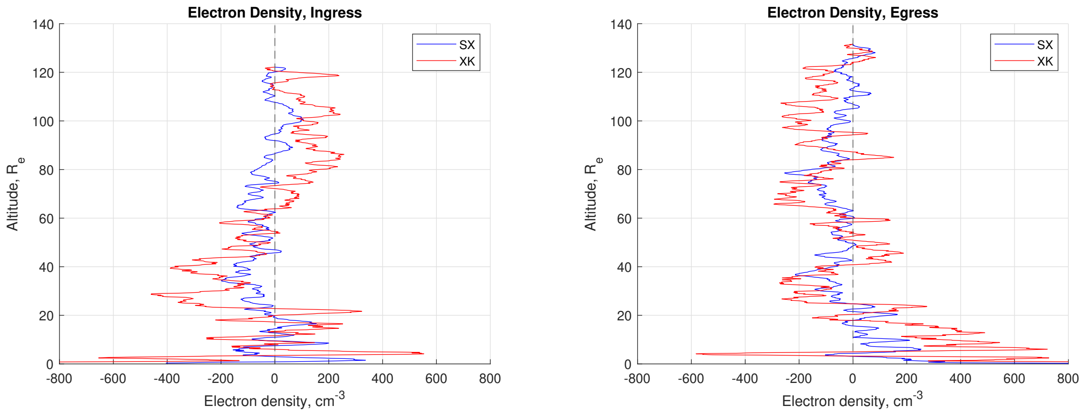

(a) Linear correction, ingress. (b) Linear correction, egress.

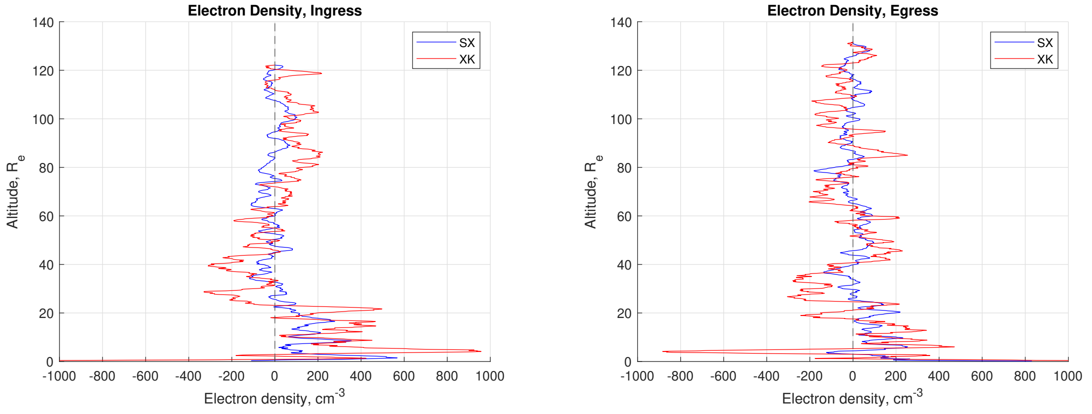

(c) 4th-degree correction, ingress. (d) 4th-degree correction, egress.

Figure 4.5: Electron density profiles from cylindrical Abel transform, 2010 occultation.

Correction	1-deg				4-deg			
Band couple	S-X		X-Ka		S-X		X-Ka	
Ingress (i)/Egress (e)	i	e	i	e	i	e	i	e
σ_{N_e} [cm^{-3}]	**84**	**89**	**205**	**217**	**92**	**79**	**200**	**183**

Table 4.1: Electron density uncertainties from standard deviation of results at high altitudes, 2010 occultation.

methodology, the usual procedure for the determination of the uncertainties is to calculate the standard deviation of the electron density measurements above a limit altitude [4]. The determination of the threshold altitude for our observation has been performed considering the geometry of the occultation: as the plumes to be observed are located in the South Polar region of the moon and they develop vertically, it could be reasonable to consider as "disturbances" all the phenomena occurring when the points of closest approach to Enceladus are located far from polar latitudes. Analysis of the occultation geometry using SPICE routines revealed that, for large distances from the moon, all the points of closest approach were located at latitudes within 5 degrees from the equator. Polar latitudes were only reached when the signal achieved the smallest distances from the celestial body, as Figure 2.1a suggests. The threshold altitude has been set as 5 Enceladus radii, the point at which the closest approach reached a latitude of 10°S and started moving towards the South Polar region. The estimated uncertainties are reported in Table 4.1: the standard deviation values measurements obtained from X- and Ka-bands, ranging from 183 to 217 cm^{-3}, are more than double the respective values calculated from S- and X-bands, which oscillate around 79-92 cm^{-3}. Relevant variations of electron density towards negative values, especially for the X- and Ka-band measurements, seem to suggest that the actual uncertainties are higher than these figures. An expression of the uncertainties in the electron density obtained by radio occultation experiments has been found by Withers as [18]:

$$\sigma_{N_e} = \frac{20\pi\sigma_{\Delta f} f c m_e \varepsilon_0}{|v_\perp| e^2}\sqrt{\frac{dz}{2R}} \tag{4.1}$$

where $\sigma_{\Delta f}$ is the uncertainty in the frequency residual values, $|v_\perp|$ the norm of the component of the spacecraft velocity which is orthogonal to the spacecraft-Earth line of sight, in the frame of reference of the occulting body, dz the vertical resolution, and R the radius of the occulting body. Although this expression cannot be directly utilized for our analysis, as our approach did not include the calculation of frequency residuals, it may still provide some insight into the behavior of electron density measurement errors. Most of the terms in Equation 4.1 are constant during the experiment, including $\sigma_{\Delta f}$ and f, as variations in frequency are negligible when multiplying, whereas the varying terms are the norm of the orthogonal component of the spacecraft velocity and the radical. The latter is the result of an approximation: the actual term that should appear at the denominator is X_j, which is the impact parameter of the j-th ray, generally assumed to be close to the planetary radius to obtain a constant value of electron density uncertainty, valid for the whole experiment. This assumption holds for the analysis of planetary atmospheres, as the radius of the planet significantly exceeds the atmospheric thickness. However, this hypothesis is not applicable for the analysis of a satellite like Enceladus, whose diameter is a small fraction of that of a gas giant. $|v_\perp|$ can be evaluated using SPICE routines: this quantity varies throughout the experiment, ranging from a maximum value of 14.7 km/s at the beginning of the observation, to a minimum of 11.1 km/s when the radio science activity ended. For the purpose of this analysis, the variation of $|v_\perp|$ can be considered as negligible, since approximations are already present when using this model to estimate electron density uncertainties. These approximations are mainly due to the assumption that measurement errors when combining two sets of frequency data behave similarly to those in a methodology that relies on frequency residuals. Although this hypothesis sounds rea-

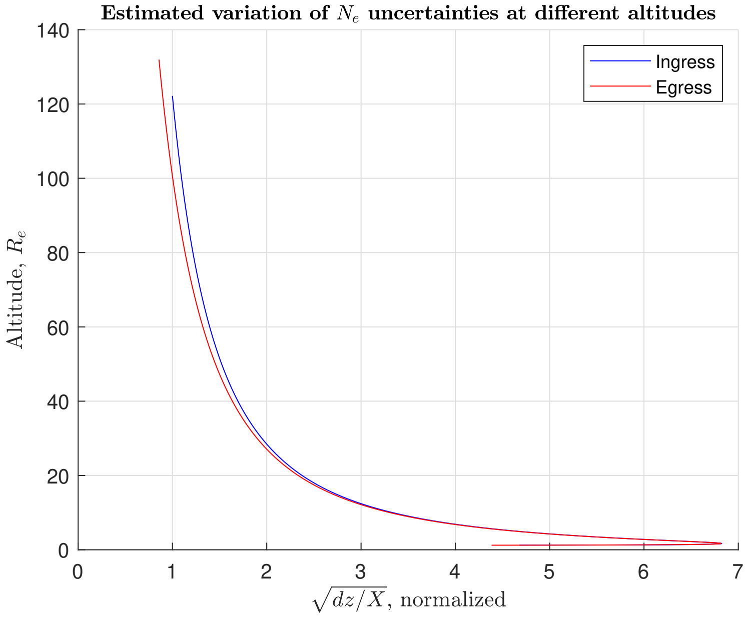

Figure 4.6: Estimation of the variation of N_e uncertainty with respect to altitude, 2010 occultation.

sonable, verifying it thoroughly can be challenging. Assuming that $|v_\perp| \approx const$, the only varying term in Equation 4.1 is $\sqrt{dz/2R}$: as a result, we may assume that $\sigma_{N_e} \propto \sqrt{dz/X}$, substituting the distance of closest approach to the planetary radius as discussed earlier.

The radical function in question is plotted against altitude in Figure 4.6. To make the result clearer, the function has been normalized by dividing it by the value of the function at the first time instant. This value tends to increase when approaching Enceladus, exceeding 4.5 at altitudes lower than 5 Enceladus radii and peaking at 6.8. This result suggests that, according to this model, σ_{N_e} in the vicinity of the satellite is more than 4.5 times the value at the highest altitude, reaching a peak of nearly 7 times the original uncertainty. Estimation of the uncertainties listed in Table 4.1 has been performed by determining the standard deviation of all density measurements above an altitude of 5 Enceladus radii: since the measurement errors tend to significantly increase at lower altitudes, this approach may underestimate variabilities at closer distance to the moon. A procedure that considers the effect of increasing uncertainties consists of computing the standard

Correction	1-deg/4-deg			
Band couple	S-X		X-Ka	
Ingress (i)/Egress (e)	i	e	i	e
σ_{N_e}, high alt. [cm^{-3}]	49	50	103	98
σ_{N_e}, low alt. [cm^{-3}]	**221-343**	**225-350**	**464-721**	**441-686**

Table 4.2: Estimated electron density uncertainties at low altitudes, 2010 occultation.

deviation at high altitudes, in a range which is large enough to average out local effects, and small enough to avoid relevant increments of uncertainties associated with decreasing altitude, and then multiplying this value by the corresponding increasing factors for each altitude. The interval of altitudes higher than 80 Enceladus radii seems to satisfy the described conditions, as the increments related to the distance from the planet are within 20%, and the computed standard deviation does not experience large variations with slight modifications of the interval. Results of this operation are shown in Table 4.2, where the uncertainties at low altitudes have been computed multiplying by factors from 4.5 to 7 the corresponding quantities obtained using altitudes above 80 Enceladus radii. The derived amounts are almost not affected by the correction strategies applied to the total electron content. Overall, the estimated measurements errors are comparable to the absolute values of the inferred electron densities, indicating that noise has highly affected the observation. As a result, no clear conclusions regarding the ionospheric environment of Enceladus and the characteristics of its water plumes can be addressed from this analysis.

4.2 Results of 2006 occultation

The same process has been conducted for the radio signals received during the Enceladus occultation of September 15, 2006: although this observation did not cover the South Polar region of the satellite, the analysis of the experiment in question has been considered to per-

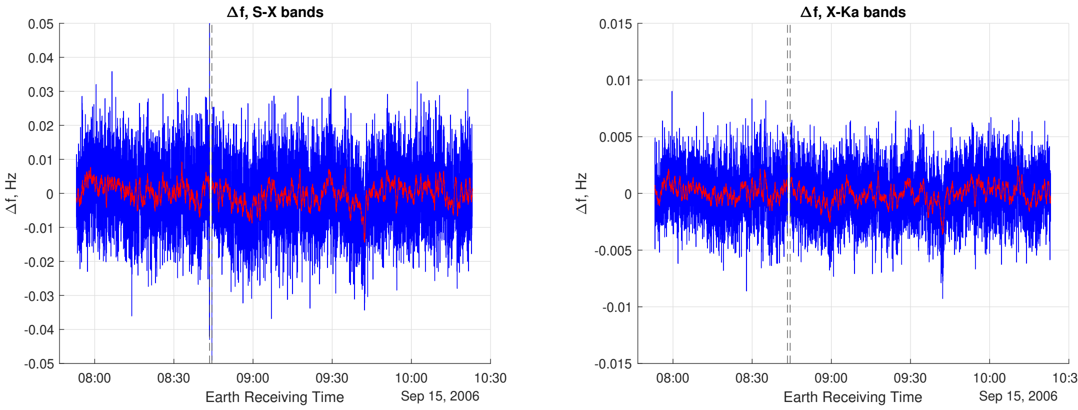

(a) S- and X-bands. (b) X- and Ka-bands.

Figure 4.7: Δf of the occultation of September 15, 2006.

form a complete study of the observations of the icy moon by Cassini. The time series of frequency differences Δf_{SX} and Δf_{XK} are shown in Figure 4.7, where the blue lines represent the computed Δf sequences, and the red line the averaging in time of the results, obtained performing the mean in a moving time window of 28 seconds. Interestingly, the oscillations in the Δf values of the S- and X-band couple are more intense than those of its counterpart: the standard deviations $\sigma_{f,SX}$ and $\sigma_{f,XK}$ are, respectively, equal to 9.7 mHz and 2.2 mHz, the latter value being comparable to the standard deviations of the Δf measurements from the 2010 occultation. The higher standard deviation of Δf_{SX} can be explained by the significantly lower signal to noise power ratio of the received S-band signal (see Figure 2.9). Overall, the two graphs represent similar trends, characterized by oscillations around zero, with absolute values of Δf smaller than 0.03 Hz for the S- and X-band signals couple, and smaller than 7 mHz for the couple formed by X- and Ka-band signals, with the exception of some outliers. Both the Δf experience analogous oscillations, distributed throughout the entire observation window, regardless of the proximity of the signal to Enceladus. Analogously to the 2010 occultation, the sampling rate selection has a negligible effect on the Δf calculation.

Using the procedure described in section 3.1, the time sequences of frequency differences have been utilized to infer the total electron content

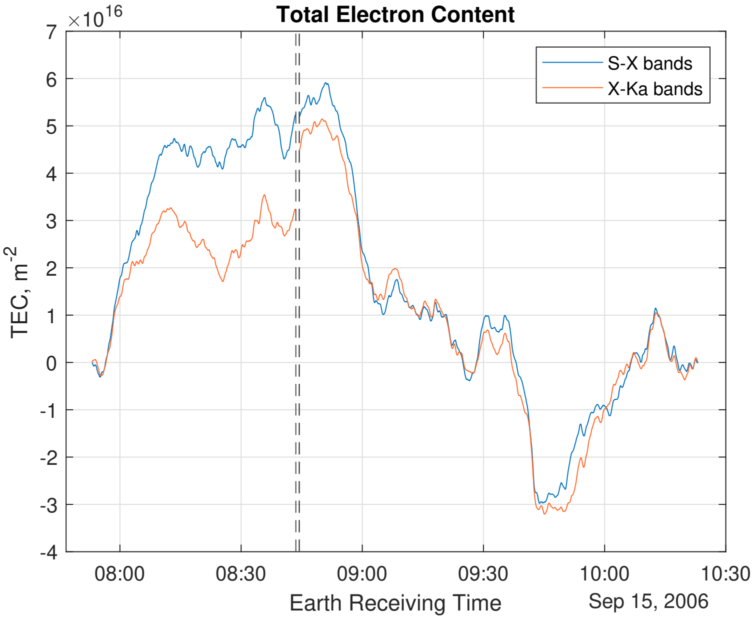

Figure 4.8: Total electron content before correction of Δf, 2006 occultation.

encountered by each ray during the experiment: the outcome of this process is reported in Figure 4.8. To improve the visual representation, two constant values were subtracted from the total electron content measurements in both the ingress and egress branches, ensuring that the quantity becomes zero at the first and last time instants. This operation does not affect the analysis because the total electron content is obtained through an integration, which includes an arbitrary additive constant. The output of the integration of the two Δf measurements follow similar trends, mostly ascending in the ingress segment and descending in the egress segment. Significant similarities are noticeable in the total electron content oscillations of the egress branch. On the other hand, the ingress segment of the experiment displays similar variations in the two results, although the magnitude of these effects is more pronounced for the samples related to the S- and X-band couple. The overall variation of total electron content in the ingress branch is around $6 \cdot 10^{16}$ m^{-2} for the samples obtained by S- and X-band signals and $3 \cdot 10^{16}$ m^{-2} for the X- and Ka-band couple, while, for the egress branch, both the outcomes vary in a range of $9 \cdot 10^{16}$

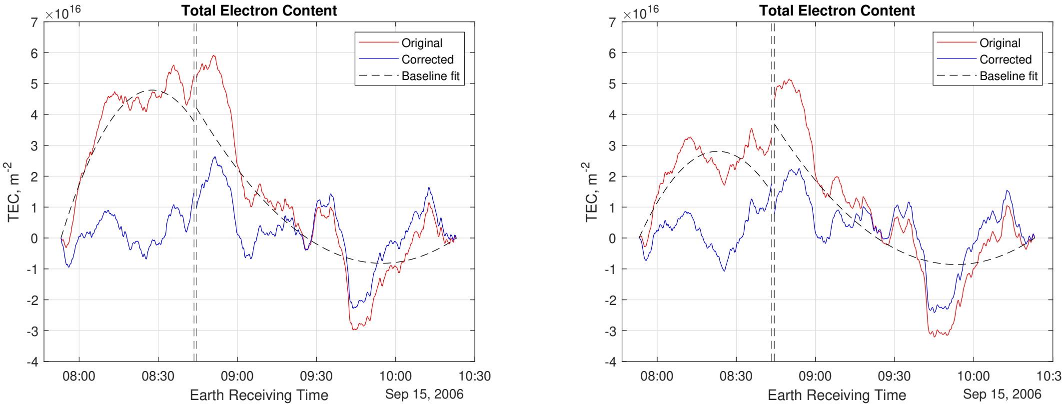

(a) S- and X-bands.

(b) X- and Ka-bands.

Figure 4.9: Total electron content after linear correction, 2006 occultation.

m^{-2}. These intervals of variation are considerably larger than those experienced by the total electron content results of the 2010 occultation (Figure 4.2). Corrections to the raw Δf measurements have been tested. Unlike in the previous case, employing linear corrections computed within a baseline located at a sufficient distance from Enceladus could provide more favorable results. The outcome of this procedure is reported in Figure 4.9: the corrected total electron content profiles experience variations around a zero value, with positive peaks near the celestial body. However, linear corrections do not significantly impact the largest oscillations, as some of them maintain values analogous to the peaks near Enceladus. In contrast to the 2010 occultation, the usage of polynomial corrections did not yield meaningful results.

The corrected total electron content expressions have been used to estimate electron density profiles, which are shown in Figure 4.10. Each profile experiences divergence at low altitudes, either towards positive or negative values, which does not originate from numerical instabilities occurring when computing the integral. The oscillations in the electron density values are significantly more intense than those measured in the 2010 occultation, presented in section 4.1. Figure 4.10 suggests the presence of electron densities as high as 2000 cm^{-3} at altitudes around 20 to 40 Enceladus radii, which were not detected in the

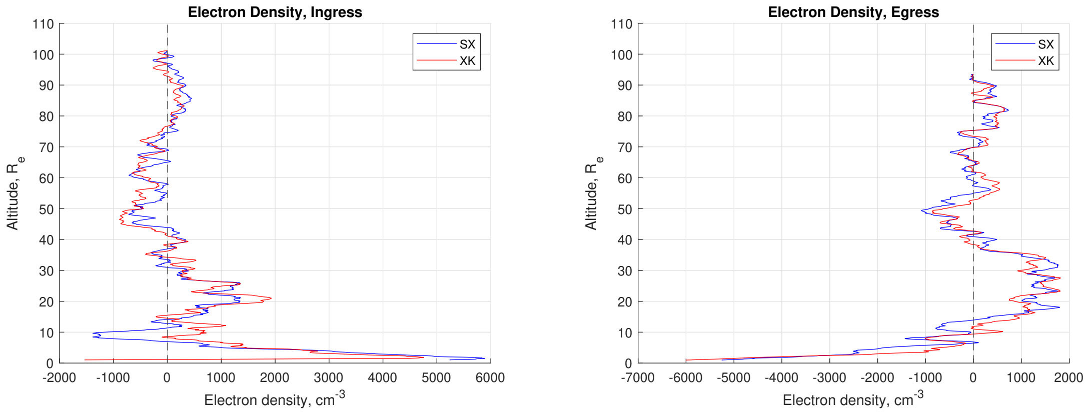

(a) Ingress. (b) Egress.

Figure 4.10: Electron density profiles from cylindrical Abel transform, 2006 occultation.

2010 occultation, when similar locations were scanned before the rays reached the South Pole of the satellite. Equation 4.1, which defines the uncertainties in the measurements of N_e inferred from frequency residuals, can be used as a reference for the estimation of our measurement errors: as already seen in section 4.1, all the terms in the equation are almost constant, except $\sqrt{dz/X}$. Figure 4.11 shows the behavior of the term in question, which can be assumed as proportional to the measurement error, with respect to altitude. The picture shows a rapidly increasing trend at low altitudes: values from 4 to 9 times the uncertainty at the maximum height of the observation are reached at altitudes lower than 5 Enceladus radii. The standard deviation of measurements taken at altitudes over 50 Enceladus radii, where uncertainties vary within 30% of the original value due to the estimated effect of vicinity to the satellite, has been calculated and then multiplied by 9 to assess the uncertainties of measurements near the satellite. Table 4.3 reports the results of this operation, showing that the uncertainty levels are sensibly higher than those of the Enceladus occultation that occurred in 2010 (see Table 4.2). Diverging values for the electron density at low altitudes suggest that measurements taken at very low altitudes are unreliable. Electron densities at altitudes between 20 and 40 Enceladus radii reach values higher than the

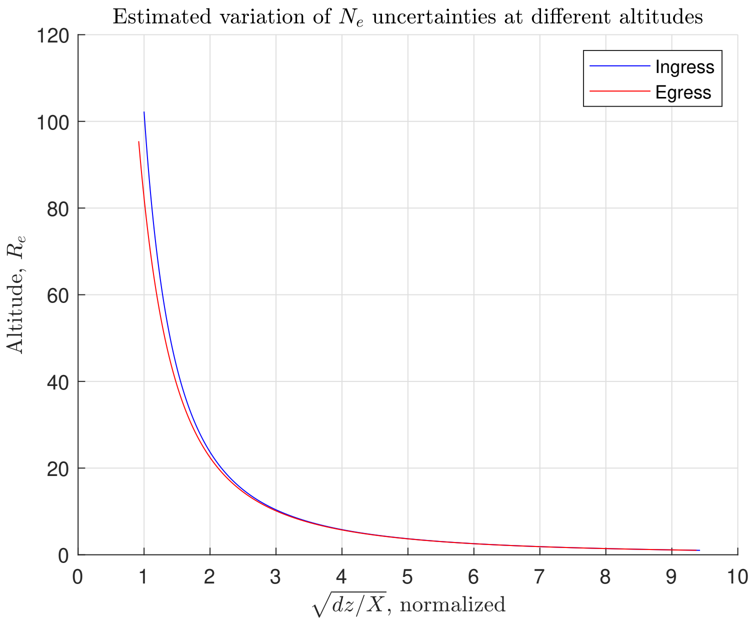

Figure 4.11: Estimation of the variation of N_e uncertainty with respect to altitude, 2006 occultation.

Band couple	S-X		X-Ka	
Ingress (i)/Egress (e)	i	e	i	e
σ_{N_e}, high alt. [cm^{-3}]	326	392	295	330
σ_{N_e}, low alt. [cm^{-3}]	$\sim$ **2900**	$\sim$ **3500**	$\sim$ **2700**	$\sim$ **2900**

Table 4.3: Estimated electron density uncertainties at low altitudes, 2006 occultation.

correspondent noise level, according to this model: Figure 4.11 suggests that, in the interval in question, uncertainties in N_e are less than twice the value calculated at high altitudes, resulting in σ_{N_e} figures smaller than 800 cm^{-3}, whereas densities reach 2000 cm^{-3}. However, these high densities would likely have been observed during the following occultation in 2010, which had considerably lower noise levels. Therefore, it is reasonable to assume that the inferred high densities are an artifact of noise, indicating that measurement errors are even higher than originally supposed.

Chapter 5

Simulation of the observables

This chapter illustrates electron density models for the ionospheres of Saturn and Enceladus and the methodology used to simulate the effects of these quantities on total electron content and Δf resulting from radio occultation experiments.

5.1 Methodology

By definition, the total electron content Ω is the integral of the electron densities encountered by a radio wave during its propagation. Dividing the ray path in an arbitrary number of segments of length Δl, this quantity can be numerically approximated as:

$$\Omega_i = \Omega(t_i) = \int_i N_e dl \approx \sum_j N_e(i,j)\Delta l \tag{5.1}$$

where t_i is the transmission time of the i-th ray, $N_e(i,j)$ the local electron density of the j-th segment of the i-th ray, and the symbol $\int_i$ indicates that the integration is performed over the trajectory of the i-th path. For the results reported in this chapter, $N_e(i,j)$ is calculated utilizing electron density models which are dependent on the relative position of the j-th segment of the i-th ray with respect to Enceladus or Saturn. The propagation of the electromagnetic wave is performed along the Cassini-Earth line of sight $\hat{n}$, considering the movement of the planet during the signal travel time. From the time sequence of total electron content, the observable Δf can be estimated by approximating Equations 3.5 and 3.6:

$$\Delta f_i = \Delta f(t_i) = \gamma \frac{d\Omega}{dt} \approx \gamma \frac{\Omega_{i+1} - \Omega_{i-1}}{2\Delta t} \tag{5.2}$$

where γ groups all the constant terms. The structure of the algorithm is the following:

1. The observation period and the time resolution Δt are selected, defining a sequence of equally spaced time instants t_i;
2. A space resolution Δl for the length of the ray segments is defined;
3. The relative positions of Cassini, the Earth, and the celestial bodies necessary for the electron density model in question (Saturn of Enceladus) are calculated at time t_i utilizing SPICE routines;
4. Starting at the Cassini position at time t_i, $\bar{x}_{i,0}$, the ray position is propagated towards the Earth direction: $\bar{x}_{i,j} = \bar{x}_{i,j-1} + \Delta l \hat{n}$;
5. $N_e(i,j)$ is computed, using the relative position between $\bar{x}_{i,j}$ and Saturn/Enceladus according to the density model in question;
6. j is incremented, the algorithm resumes from step 4, until a stop condition on the value of N_e or on the distance between the ray and Saturn/Enceladus is fulfilled;
7. Ω_i is calculated using Equation 5.1;
8. Δf_i is calculated using Equation 5.2 (except at the first and last time instants);
9. i is incremented, the algorithm resumes from step 3, until the end of the observation window.

In the next sections, Δf estimates are only provided for the S- and X-band frequency couple. The analysis presented here neglects instrumental noise and plasma wind effects, eliminating frequency-dependent components. Consequently, the two frequency difference outcomes only vary by a multiplicative factor. The constants in Equation 5.2 are $\gamma_{SX} = 5.41 \cdot 10^{-17}$ m^2 and $\gamma_{XK} = 1.49 \cdot 10^{-17}$ m^2, where the unit, although lacking physical meaning, is required for consistency. Comparing the two constants reveals that $\Delta f_{SX} = 3.65 \Delta f_{XK}$.

5.2 Saturn ionosphere

Enceladus orbits Saturn at an average distance of 238,000 km, or approximately 3.95 Saturn radii (R_S). Radio signals transmitted from Cassini during the Enceladus occultations in question may have been affected by the ionosphere of Saturn. This section addresses the impact of electron density variations in the ionosphere of Saturn on the radio waves during occultation experiments. Total electron content and Δf derived from this analysis are compared to the radio occultation results, to determine whether this effect constitutes a relevant source of noise in our experiment, and, if so, to apply correction to the observed quantities based on this result. The methodology described in section 5.1 has been utilized for two models of Saturn's ionosphere, with results presented in the next subsections.

5.2.1 Holmberg model for equatorial Saturn electron densities

Holmberg et al. [6] developed models of ion and electron densities in the ionosphere of Saturn, based on Cassini Radio and Plasma Wave Science (RPWS) measurements. These models, shown in Figure 5.1, provide estimates for N_e and other ions as a function of radial distance from Saturn, up to 12 R_S. Figure 5.1 illustrates density peaks at a distance of 4.6 R_S from the planet, with electron density reaching 75 cm^{-3}. Moreover, N_e undergoes significant variations between 4 and 6 R_S, a region covered by electromagnetic rays during the occultations of Enceladus. This model is valid for the equatorial region of Saturn, within a vertical distance of 0.5 R_S from the equatorial plane. This condition is respected for the 2010 occultation, as electromagnetic waves move inside the window in question from propagation until reaching a distance of 12 R_S. On the other hand, the inclined trajectory of radio signals transmitted during the 2006 occultation makes this method not applicable for this observation. During this observation, Cassini was positioned at vertical distances of approxi-

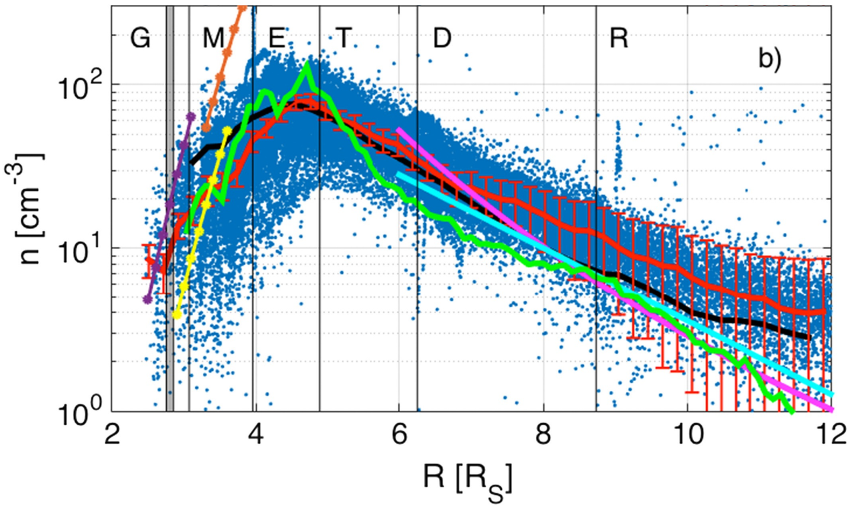

Figure 5.1: Holmberg electron density model (black line) for the equatorial regions of Saturn [6].

mately 3 R_S above the equatorial plane, and radio waves reach vertical distances of about 2.5 R_S below the equatorial plane when reaching a distance of 12 R_S from Saturn.

The numerical method defined in section 5.1 has been applied to the geometry of the 2010 occultation, using the model in Figure 5.1 for the determination of local N_e, and interrupting the ray propagation when a distance of 12 R_S from Saturn is reached. The integration step Δl for the propagation of the signal has been set at 10 km, a value which allows for both a proper resolution in the inferred quantities and an appropriate computational time. Results shown in Figure 5.2 reveal gradual variations in total electron content, for a total of approximately $2 \cdot 10^{15}$ m^{-2} over the whole experiment period. This effect is one order of magnitude smaller than the total electron content reconstructed from the observed frequencies, reported in Figure 4.2. Similarly, the simulated Δf generated by this N_e model is in the order of 10^{-5} Hz, considerably smaller than the frequency uncertainties. As a result, the Holmberg electron density model suggests that the ionosphere of Saturn had minimal impact on the radio occultation of Enceladus conducted by Cassini in 2010.

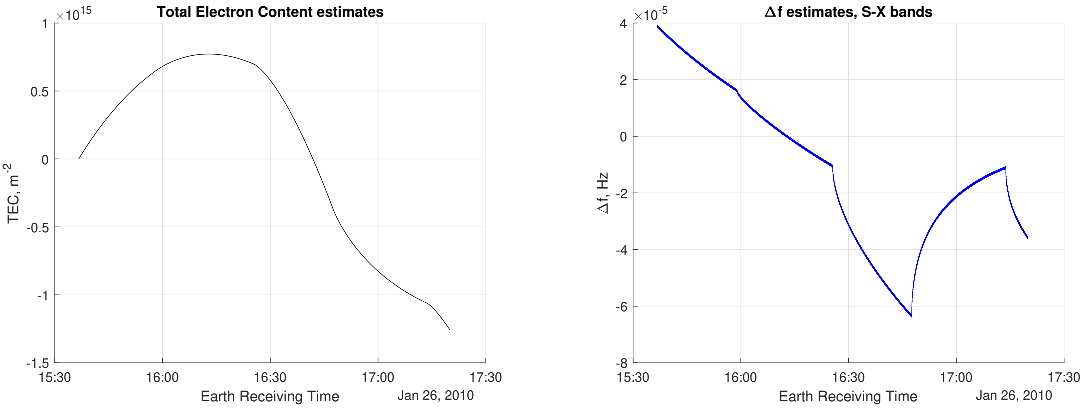

(a) Total electron content. (b) Δf, S-X bands.

Figure 5.2: Estimated effect of Saturn ionosphere on total electron content and Δf for the 2010 occultation, Holmberg density model.

5.2.2 Persoon model for Saturn electron densities

A second model for ion and electron densities in the ionosphere of Saturn has been developed by Persoon et al. [8]. This model is based on RPWS measurements, like the previous one, and on the solution of equilibrium equations, specifically diffusive equilibrium equations, which account for numerous effects in Saturn's ionosphere, including centrifugal forces resulting from the rotation of the planetary magnetosphere. The resulting electron density distribution is depicted in Figure 5.3, illustrating values as a function of both distance from Saturn on the equatorial plane (ρ) and vertical distance from the equatorial plane (z). Estimates for N_e are available for ρ values smaller than 10 R_S and $|z|$ values smaller than 4 R_S. Results on the equatorial plane align with those reported by Holmberg et al., while density reductions are notable as $|z|$ increases.

Numerical evaluation of total electron content and Δf for the 2010 occultation has been conducted using the electron density model of Persoon. Similarly to the analysis conducted using the Holmberg model, the usage of a resolution Δl of 10 km guarantees adequate resolution in a relatively short computational time. Results in Figure 5.4 indicate a total electron content variation of about $6 \cdot 10^{14}$ m^{-2} over the entire experiment duration. This value is smaller than that obtained with

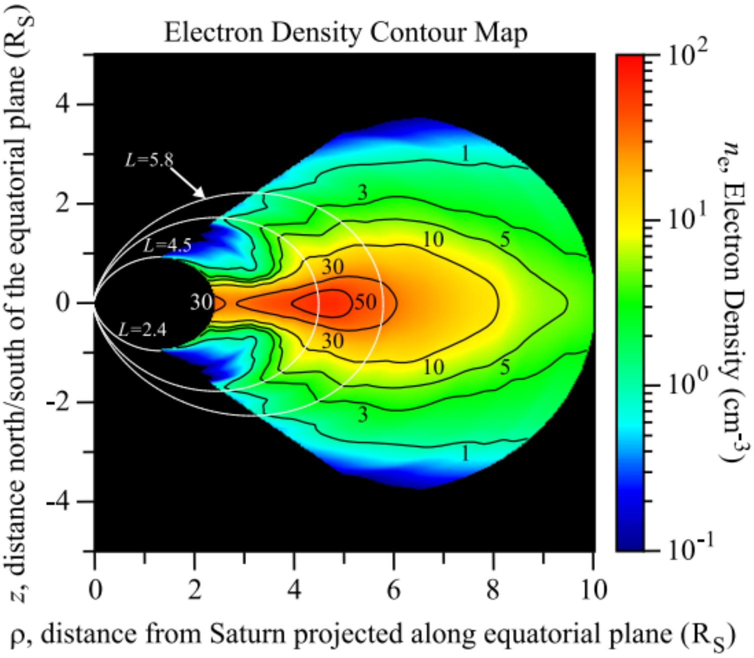

Figure 5.3: Persoon electron density model for the ionosphere of Saturn [8].

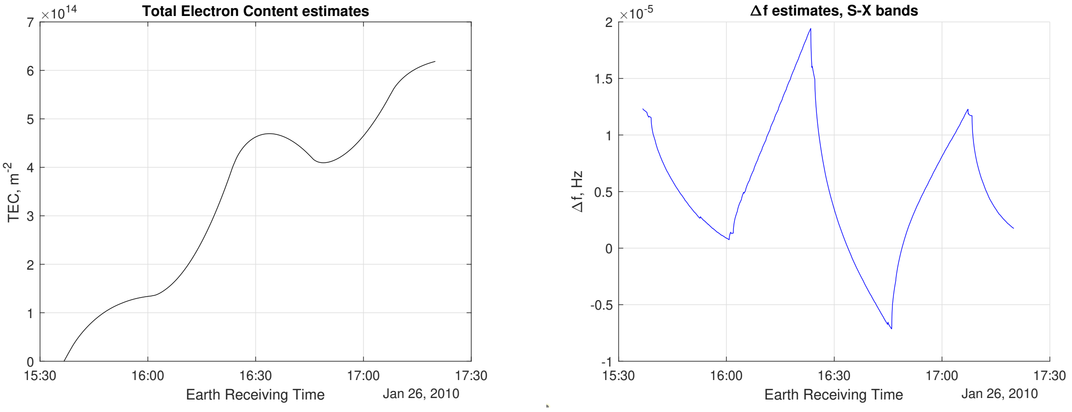

(a) Total electron content.

(b) Δf, S-X bands.

Figure 5.4: Estimated effect of Saturn ionosphere on total electron content and Δf for the 2010 occultation, Persoon density model.

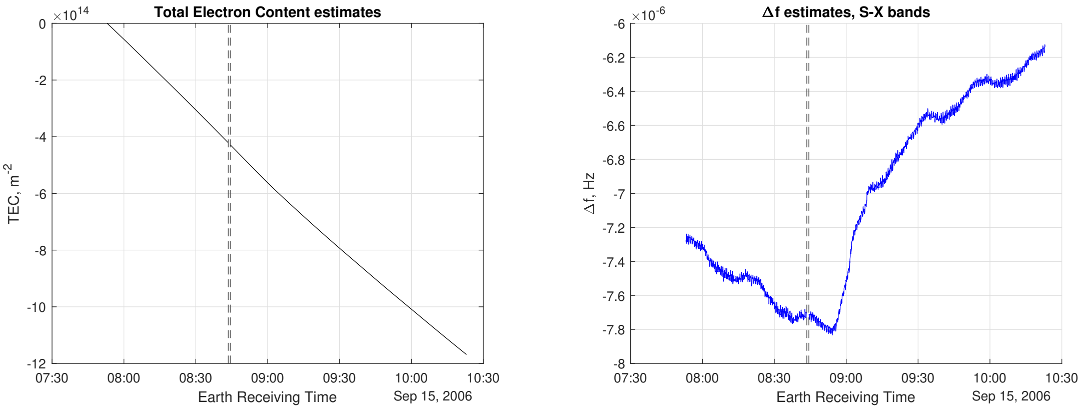

(a) Total electron content.

(b) Δf, S-X bands.

Figure 5.5: Estimated effect of Saturn ionosphere on total electron content and Δf for the 2006 occultation, Persoon density model.

the Holmberg model and negligible with respect to the observed TEC. Accordingly, Δf estimates range in the order of 10^{-5} Hz, suggesting that this effect would not be detectable.

The presence of measurements at distance from the equatorial plane of Saturn allows for the estimation of the same quantities during the radio occultation of 2006. Result in Figure 5.5 demonstrate that, also for this observation, the ionosphere of Saturn did not considerably affect the occultation, as the overall variation in total electron content is in the order of 10^{15} m^{-2}, while the observed TEC variations are more than 10 times more intense. The inferred Δf is in the order of μHz, which is orders of magnitude lower than the frequency uncertainties in that observation.

The negligible magnitude of all total electron content and Δf results reported in this section reveals that Saturn ionosphere did not constitute a significant source of noise for the occultation experiments, despite the relevant variations in electron densities along the signal paths.

5.3 Enceladus ionosphere

Simulations of theoretically observable total electron content and Δf measurements have been conducted. These simulations were based on N_e measurements around Enceladus collected from other studies, and on water plume density models. The analysis aims to verify the compatibility between existing measurements and the results of radio occultations conducted by Cassini.

5.3.1 Radio and Plasma Wave Science (RPWS) measurements

The RPWS instrument on-board Cassini collected electron density measurements during its fly-bys of Enceladus. Figure 5.6 displays N_e quantities measured during the 14 equatorial fly-bys of the satellite from 2005 to 2015. Except for E20 (black line), which was a North Pole observation, all fly-bys occurred in the proximity of the South Pole of Enceladus. Measurements are available at distances smaller than 200 Enceladus radii (R_E), until closest approaches of around 2 R_E for most observations. No data is available when closer than 1.3 R_E, as water ice particles generating from the cryovolcanic activity of Enceladus tend to impact with antennas, invalidating measurements [21]. Relevant variabilities are visible among different sets of data, with electron densities ranging from 20 to 80 cm^{-3} at large distance from Enceladus. A general increasing trend can be observed when approaching the satellite, with densities reaching 40-130 cm^{-3} for the last available measurements. This variability is attributed to the complex interactions between particles in the Enceladus environment, including electron absorption by negative ions and icy particles [5]. A correlation between electron densities and the orbital anomaly of Enceladus has been identified. Electron densities experience an increase when the satellite is positioned near the orbital apoaxis, at the maximum distance from Saturn. This observation can be explained by tidal stresses driving the erupting activity of the moon: these stresses are

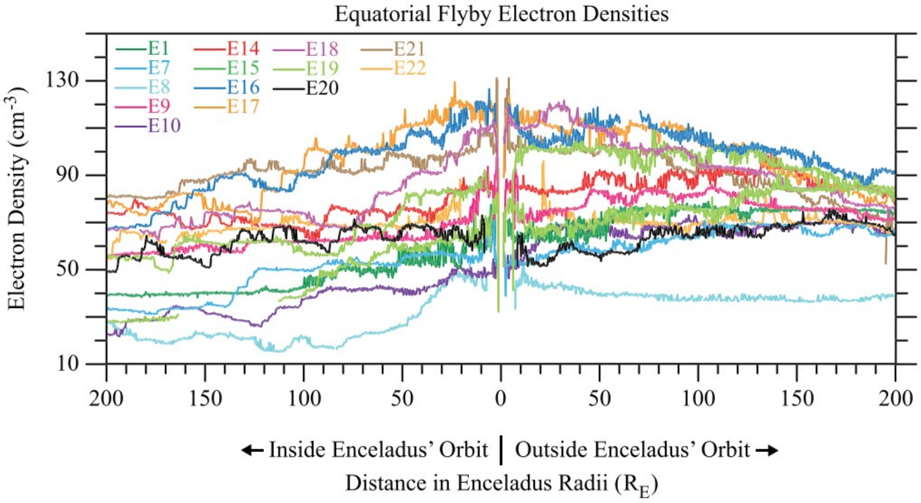

Figure 5.6: Cassini RPWS electron density measurements in the vicinity of Enceladus [9].

at their maximum near the orbital periaxis, closing the fissures in the South Polar regions of Enceladus. On the other hand, at the apoaxis, tidal stresses tend to open cracks, amplifying the emission of water particles [9].

N_e measurements collected during the equatorial flybys covering the South Pole of Enceladus have been utilized to determine the ideally observable Δf and total electron content during the occultations of the moon. Integration only considered rays moving in the range where N_e estimations are available, excluding those approaching Enceladus at closer distances, with a space resolution Δl of 10 km. Results in Figure 5.7 indicate that, for both occultations, these effects are more intense than those caused by Saturn ionosphere, but still smaller than quantities inferred by radio occultations. The estimated total electron content varies of approximately 1-6 $\cdot 10^{15}$ m^{-2}, values one order of magnitude smaller than variations measured during the 2006 occultation (3-9 $\cdot 10^{16}$ m^{-2}). Total electron content inferred from the 2010 occultation of Enceladus experienced total variations of 1-2 $\cdot 10^{16}$ m^{-2}, indicating that some of the quantities calculated from the integration are not negligible. Analysis of the Enceladus orbit using SPICE routines revealed that during both occultations the satellite was in the

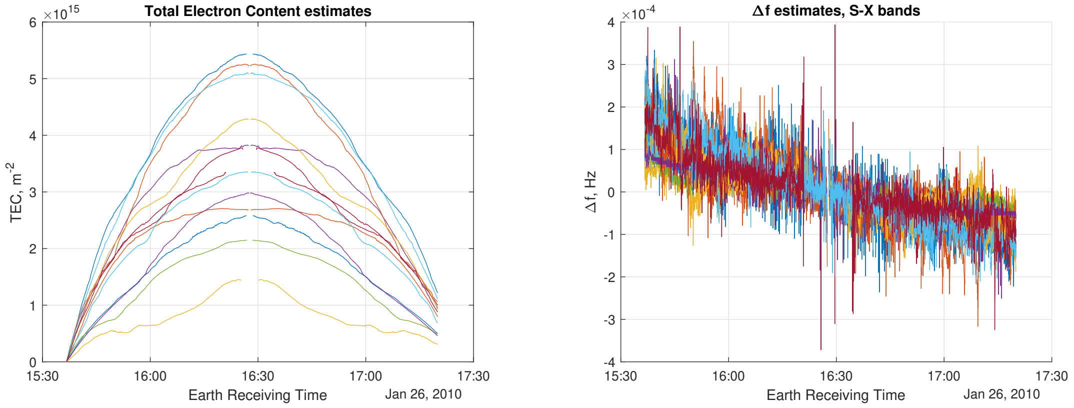

(a) Total electron content, 2010 occultation.

(b) Δf, S-X bands, 2010 occultation.

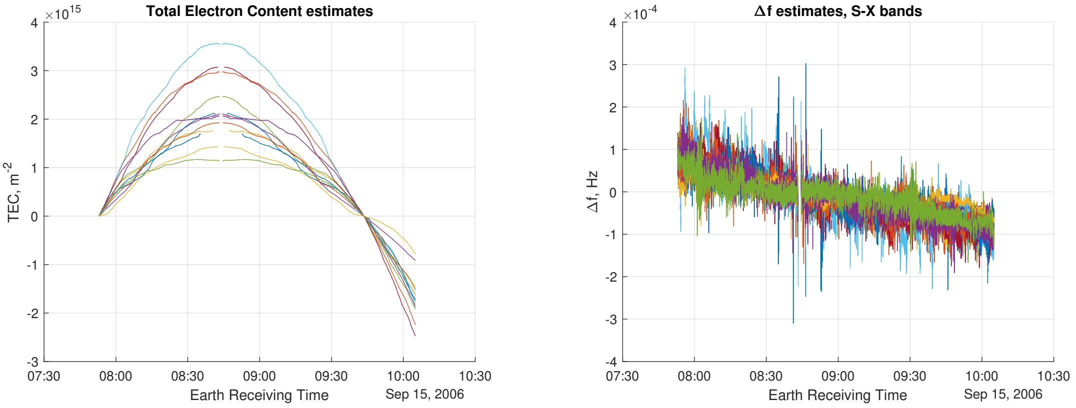

(c) Total electron content, 2006 occultation.

(d) Δf, S-X bands, 2006 occultation.

Figure 5.7: Estimated observable total electron content and Δf during the Cassini occultations using RPWS electron densities around Enceladus.

periapsis region, where cryovolcanic activity is expected to be at a minimum. By selecting only measurements collected close to the periapsis (excluding E21, characterized by higher density peaks, possibly for other reasons [9]), the inferred total electron content profiles experience variations of 1-3 $\cdot 10^{15}$ m^{-2}, one order of magnitude smaller than those measured by radio occultation frequency data. Analogously, the estimated Δf for the S- and X- bands ranges within absolute values of 0.4 mHz, below the uncertainty limits.

Reconstruction of total electron content and frequency difference estimates attributed to the plasma environment of Enceladus reveals that these features, at least at distances greater than 1.3 R_E, are too small to be detected by radio occultation analysis. The absence of RPWS measurements at closer distance makes this analysis not suitable for the detection of water plumes, whose densities are expected to be more intense. The following sections present the results of the same methodology applied to N_e estimations inside the plume region and to a plume density model, to investigate the effects of these geological features on radio occultations.

5.3.2 Langmuir probe (LP) plume measurements

The Langmuir Probe (LP) was a scientific payload on-board Cassini with the goal of analyzing the in-situ plasma environment. Morooka et al. [7] reported electron density estimates within Enceladus plumes, derived from LP voltage sweep data collected during four Enceladus fly-bys (E3 to E6) in 2008. Figure 5.8 reports N_e estimates during the E3 encounter, indicating the presence of significant density drops before the closest approach, in a ”wake” region formed by the revolution motion of Enceladus, as well as electron density peaks of 2000-4000 cm^{-3} in the plume region. At larger distances, N_e quantities align with RPWS measurements presented in subsection 5.3.1. Electron density estimates from the other Enceladus encounters (E4-E6) highlight similar trends.

These measurements have been employed for numerical integration

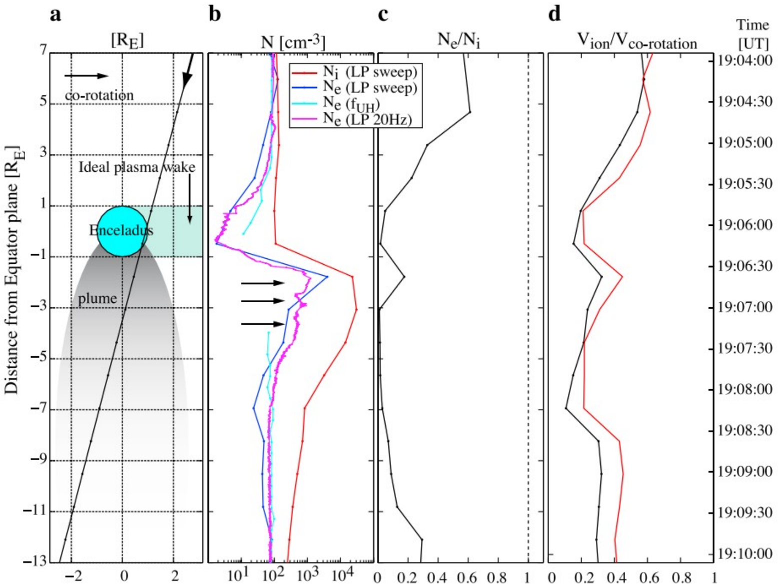

Figure 5.8: Electron density in the vicinity of Enceladus from LP voltage sweep data (blue and magenta lines), Enceladus E3 fly-by [7].

of total electron content and Δf which would have been observable when radio signals passed by the Enceladus South Pole. Seven electron density models have been created for this purpose, using one of the RPWS dataset extending until the closest distances to the moon (E7, E9, E14, E17, E18, E19, E21) for N_e estimation at large distances. When electromagnetic rays reached distances from the rotation axis smaller than a threshold value $\rho_{lim} = 2R_E$, the model employed LP estimates, providing N_e as a function of vertical distance from the Enceladus equatorial plane. Different values of ρ_{lim} have been tested, resulting in minor changes in the obtained results. An adaptive integration step has been utilized, with Δl set to 10 km at large distance from Enceladus and reduced to 1 km in the plume region, to more accurately estimate the effects of this narrow region on radio occultation observables. Figure 5.9 illustrates the outcome of this procedure in terms of total electron content and Δf. As expected, the only notable differences with respect to the quantities inferred only using RPWS measurements (Figure 5.7) occur in a one-minute time window around the point of closest approach. Higher electron densities in the plume result in total electron content peaks approximately 10^{14} m^{-2}

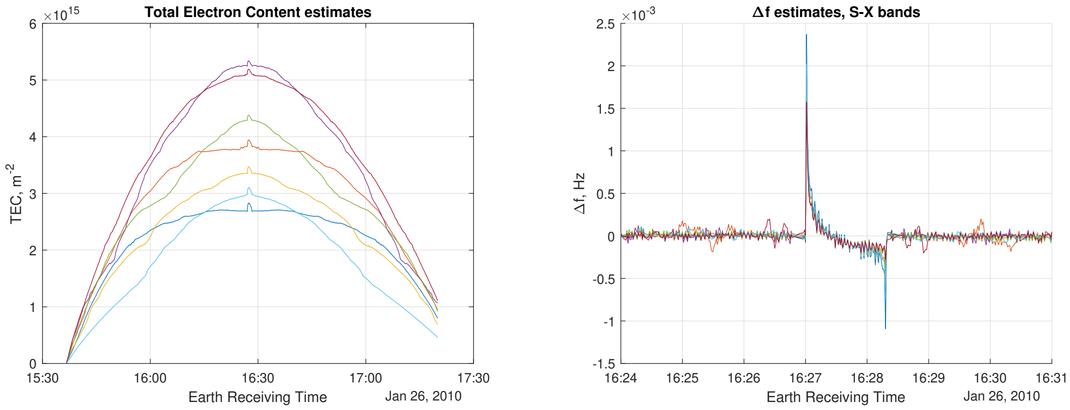

(a) Total electron content. (b) Δf, S-X bands.

Figure 5.9: Estimated observable total electron content and Δf during the Cassini occultations using LP measurements for plume densities.

higher than the values obtained from integration of RPWS densities. These features occur in a narrow time window, resulting in Δf estimates that peak at 1.6-2.4 mHz, values significantly higher than those inferred outside of the plume region but still comparable to measurement uncertainties ($\sigma_f = 2.5$ mHz for the S-X band couple). The analysis in question involved switching between two density models at a fixed distance, potentially resulting in abrupt N_e changes and lower accuracy in the inferred quantities. Moreover, it is worth noting that all the fly-bys used for the estimation of electron densities in Figure 5.8 occurred when the satellite was orbiting Saturn in its post-apoapsis orbital region, where more intense cryovolcanic activity is expected. Hence, this analysis may overestimate the actual N_e encountered during radio occultation of Enceladus plumes.

5.3.3 Saur models for plume densities

Saur et al. [12] developed mathematical models for neutral densities in Enceladus plumes. Although these models were originally intended for a different quantity, one may assume that electron and neutral densities maintain approximately proportional inside plumes. The resulting N_e expression as a function of radial distance from the Enceladus center r and angular distance from the plume axis θ reads:

$$N_e(r,\theta) = N_0 \left(\frac{R_E}{r}\right)^2 \exp\left[-\left(\frac{\theta}{H_\theta}\right)^2\right] \exp\left(-\frac{r-R_E}{H_d}\right) \tag{5.3}$$

where N_0 is the maximum density located at the plume center on the surface of Enceladus, H_θ is the plume angular width, and H_d is a height scale. Equation 5.3 consists of exponential decays of density with increasing altitude and angular distance. A simple model for Enceladus water jets consists of a single plume located at the South Pole of the satellite with an angular width H_θ of 12°. The value of H_d, regulating the intensity of altitude decay, has been established by Saur et al. based on interactions between neutral particles and Saturn gravity. In our case, modifying H_d has little effect on results since θ varies more rapidly than r along the ray trajectory. To simplify the expression, the exponential component of N_e decay with altitude has been removed by setting $H_d \to \infty$, resulting in a quadratic reduction of electron density with increasing altitudes. This adjustment provides electron densities which better align with LP density estimations described in subsection 5.3.2. The maximum plume density N_0 has been set to 4000 cm^{-3}, consistent with the maximum density measured in-situ by the Langmuir Probe. A more elaborate multi-jet model has been developed, consisting of eight jets located on the tiger stripes of Enceladus at coordinates found by Spitale and Porco [15], provided in Table 5.1 and illustrated in Figure 5.10. For each jet, N_0 and H_θ are design parameters, whose determination goes beyond the purpose of this project. Saur et al. determined two sets for these parameters, based on magnetic field observations collected during the E0 encounter for the first set and on E1 and E2 encounters for the second. Table 5.1 reports the values for N_0 and H_θ utilized in simulations. The determination of N_0 for each jet was based on the analogous neutral density terms found by Saur et al., maintaining the same proportions and ensuring that the sum of all electron densities is equal to 4000 cm^{-3}. Similar to the single jet model, the exponential decay of densi-

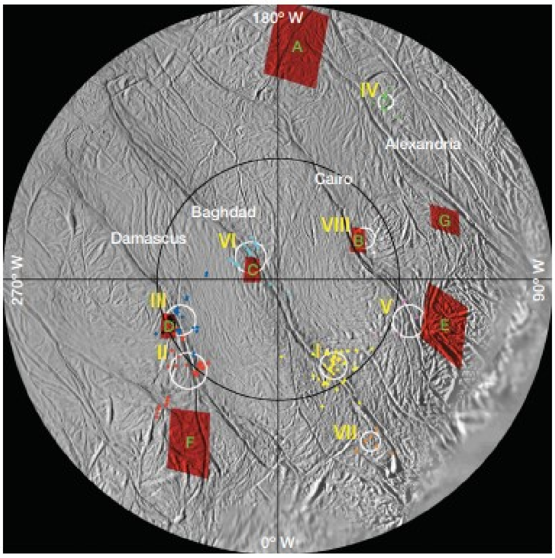

Figure 5.10: Position of jets on the Enceladus surface [15].

ties with altitude has negligible effect for our application and has been removed from Equation 5.3 by assigning an infinite value for H_d.
Simulations of total electron content and Δf caused by plumes, according to the reported models, have been performed using an integration step Δl of 1 km. At each step, the angular distance θ from each jet has been computed using trigonometric relationships and then utilized to calculate the respective N_e using Equation 5.3. The local electron density has then been obtained by summing all the contributions. Results in Figure 5.11 reveal total electron content peaks ranging from 3.5 to 5 $\cdot 10^{14}$ m^{-2} occurring in time windows from 40 seconds to one minute, depending on the jet modeling. The observable Δf for the S- and X-bands reaches maximum values from 2.5 to 3 mHz. These outcomes do not significantly differ from those obtained by integrating LP electron density measurements (Figure 5.9), indicating that the reported expression for plume density distribution is consistent with in-situ measurements. Δf peaks are slightly greater than frequency uncertainties, suggesting that the effect of jet plumes on frequency measurements would be difficult to certainly identify, considering that these phenomena interact with radio signals in a one-minute time window. Moreover, the inferred quantities in Figure 5.11

Jet locations			Multi-jet model 1		Multi-jet model 2	
Source	Lat. (°)	Long. (°)	N_0 (cm^{-3})	H_θ (°)	N_0 (cm^{-3})	H_θ (°)
I	-81.5	32.8	0	-	441	10
II	-79.4	315.5	0	-	1113	7
III	-81.3	292.8	0	-	1113	8
IV	-72.9	148.7	2233	15	0	-
V	-78.6	72.3	1767	10	0	-
VI	-87.1	231.4	0	-	1113	10
VII	-74.6	29.8	0	-	110	10
VIII	-82.1	115.5	0	-	110	10

Table 5.1: Locations of the eight jets on the Enceladus surface [15] and parameters used for simulations [12].

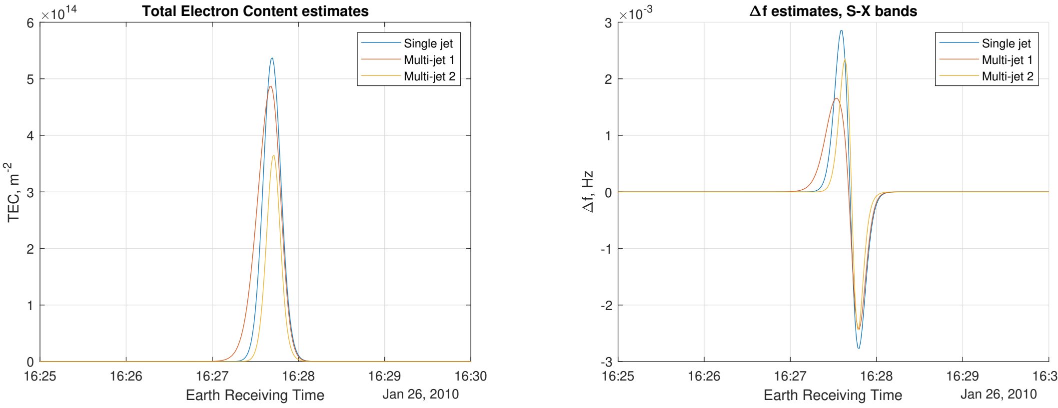

(a) Total electron content.

(b) Δf, S-X bands.

Figure 5.11: Estimated observable total electron content and Δf during the Cassini occultations using Saur models for plume densities.

are likely overestimated, as the maximum density value of 4000 cm^{-3} has been measured by the Langmuir Probe in the post-apoaxis orbital region, whereas the plume occultation was conducted in the periapsis region, when cryovolcanic activity is less intense. Jet parameters found by Saur et al. revealed notable neutral density variations. The values estimated for the E0 observation (referred to in Figure 5.11 as "multi-jet model 1") were ten times greater than those for the E1/E2 fly-bys (referred to as "multi-jet model 2"). This effect has not been included in the presented simulation: for both models, the sum of N_0 parameters has been set to 4000 cm^{-3} to estimate the maximum impact of water jets on radio occultations. Although this result cannot be directly correlated to electron density, it is reasonable to expect considerable N_e variations depending on cryovolcanic activity. Nonetheless, this analysis suggests that, considering the noise levels during the 2010 radio occultation of Enceladus plumes performed by Cassini, electron densities smaller than 4000 cm^{-3} could not have been detected.

Conclusions

The goal of the presented work was to analyze frequency data from two radio occultation experiments conducted by Cassini on Enceladus in 2006 and in 2010 to estimate electron density features within the water plumes of Enceladus and its surrounding environment. Preliminary analysis of the observation geometry revealed that the earliest occultation involved equatorial latitudes of the satellite, while the latter successfully covered the South Polar region of Enceladus, where cryovolcanic activity occurs, with a grazing occultation. Radio science signals transmitted by Cassini and received by ground station antennas were retrieved as raw files from the Planetary Data System archives, and reconstructed as time series of frequencies in the three bands utilized for scientific purposes (S-, X-, and Ka-bands). To isolate the impact of electron densities on the received signals, the frequency data for two bands at a time were combined. The outcomes of these combinations were then used to estimate the variations in total electron content over time experienced by the electromagnetic waves during transmission to the Earth. For both the occultations, total electron content results presented oscillations of comparable amplitudes spanning the entire experimental period, with no evidence of a clear peak around the time of closest approach of signals to Enceladus. Correction strategies on frequency data were tested to account for all undesired effects contributing to noise. Both the usual linear baseline correction and polynomial fits, meant to model periodic variations in the surrounding noise, provided minor improvements on results. Vertical profiles of electron density were inferred from Abel transform of total electron content, confirming the presence of high noise levels, especially during the 2006 occultation. Analysis of electron density uncertainties revealed that measurement errors rapidly increase at low altitudes due to fast variations of the impact parameter occurring when the spacecraft approaches Enceladus. This effect is negligible in the atmosphere of large planets, where the impact parameter remains approximately constant and equal to the planetary radius. Variations in the plasma environment of Saturn were examined as possible source of noise. Two models of electron density in the Saturn ionosphere were employed to simulate the potential impact of these features on radio occultation experiments. However, all results are below the uncertainty levels, suggesting that disturbances affecting the observation are attributed to system noise and possibly to variations in the interplanetary plasma. Correcting experimental results for these effects proves challenging. Examination of in-situ electron density measurements revealed that the impact of the Enceladus plasma environment on radio occultation results is too small to be detected. Measurements of electron density inside the plume region and models of density distribution inside water jets suggest that noise levels present during the Enceladus South Pole occultation of 2010 would have allowed for the detection of the crossing of those features, provided that maximum densities in the plume region are higher than 4000 cm^{-3}, a value that can be considered as an upper limit on electron density measurements derived from this study. Insitu measurements proved that such densities can be reached inside Enceladus plumes during periods of maximum cryovolcanic activity, when the satellite orbits Saturn in the post-apoaxis region. However, the radio occultation in question occurred near the Enceladus periapsis, when reductions in geological activity have been documented. Unfortunately, the density threshold determined here cannot determine the magnitude of electron density variations related to seasonal changes. Finally, this analysis revealed the potential limitations of employing radio occultation experiments for studying small satellites such as Enceladus. These experiments, being sensitive to electron density variations, have proven to provide sound results for the analysis of planets and large satellites like Titan, characterized by high densities and relatively thin atmospheres. On the other hand, Enceladus is a small body, surrounded by a diffused plasma environment, with lower densities, which makes variations of this quantity difficult to be detected, as testified by the elevated levels of uncertainties observed in this study.

Bibliography

[1] National Aeronautics and Space Administration. *Cassini*. 2022. URL: `https://www.nasa.gov/mission_pages/cassini/main/index.html`.

[2] SW Asmar et al. *Cassini Radio Science User's Guide*. 2014.

[3] JF Carbary and DG Mitchell. "Periodicities in Saturn's magnetosphere". In: *Reviews of Geophysics* 51.1 (2013), pp. 1–30.

[4] Paul A Dalba and Paul Withers. "Cassini radio occultation observations of Titan's ionosphere: The complete set of electron density profiles". In: *Journal of Geophysical Research: Space Physics* 124.1 (2019), pp. 643–660.

[5] WM Farrell et al. "Electron density dropout near Enceladus in the context of water-vapor and water-ice". In: *Geophysical research letters* 36.10 (2009).

[6] MKG Holmberg et al. "Density structures, dynamics, and seasonal and solar cycle modulations of Saturn's inner plasma disk". In: *Journal of Geophysical Research: Space Physics* 122.12 (2017), pp. 12–258.

[7] Michiko W Morooka et al. "Dusty plasma in the vicinity of Enceladus". In: *Journal of Geophysical Research: Space Physics* 116.A12 (2011).

[8] AM Persoon et al. "Distribution in Saturn's Inner Magnetosphere From 2.4 to 10 RS: A Diffusive Equilibrium Model". In: *Journal of Geophysical Research: Space Physics* 125.3 (2020), e2019JA027545.

[9] AM Persoon et al. “Evidence of electron density enhancements in the post-apoapsis sector of Enceladus’ orbit”. In: *Journal of Geophysical Research: Space Physics* 125.6 (2020), e2019JA027768.

[10] Carolyn C Porco et al. “Cassini observes the active south pole of Enceladus”. In: *science* 311.5766 (2006), pp. 1393–1401.

[11] Frank Postberg et al. “Detection of phosphates originating from Enceladus’s ocean”. In: *Nature* 618.7965 (2023), pp. 489–493.

[12] Joachim Saur et al. “Evidence for temporal variability of Enceladus’ gas jets: Modeling of Cassini observations”. In: *Geophysical Research Letters* 35.20 (2008).

[13] PJ Schinder et al. “A numerical technique for two-way radio occultations by oblate axisymmetric atmospheres with zonal winds”. In: *Radio Science* 50.7 (2015), pp. 712–727.

[14] Bradford A Smith et al. “A new look at the Saturn system: The Voyager 2 images”. In: *Science* 215.4532 (1982), pp. 504–537.

[15] Joseph N Spitale and Carolyn C Porco. “Association of the jets of Enceladus with the warmest regions on its south-polar fractures”. In: *Nature* 449.7163 (2007), pp. 695–697.

[16] Planetary Data System. *Rev 28 Satellite Earth Occultation.* 2014. URL: `https://pds-atmospheres.nmsu.edu/data_and_services/atmospheres_data/Cassini/Cassini/RSS%20PDS%20page%202019-01-23/rss/activities/657.html`.

[17] Paul Withers. “Prediction of uncertainties in atmospheric properties measured by radio occultation experiments”. In: *Advances in Space Research* 46.1 (2010), pp. 58–73.

[18] Paul Withers. “Revised predictions of uncertainties in atmospheric properties measured by radio occultation experiments”. In: *Advances in Space Research* 66.10 (2020), pp. 2466–2475.

[19] Paul Withers and L Moore. “How to process radio occultation data: 2. From time series of two-way, single-frequency frequency residuals to vertical profiles of ionospheric properties”. In: *Radio Science* 55.8 (2020), pp. 1–25.

[20] Paul Withers et al. "How to process radio occultation data: 1. From time series of frequency residuals to vertical profiles of atmospheric and ionospheric properties". In: *Planetary and Space Science* 101 (2014), pp. 77–88. ISSN: 0032-0633. DOI: `https://doi.org/10.1016/j.pss.2014.06.011`. URL: `https://www.sciencedirect.com/science/article/pii/S0032063314001822`.

[21] S-Y Ye et al. "Electron density inside Enceladus plume inferred from plasma oscillations excited by dust impacts". In: *Journal of Geophysical Research: Space Physics* 119.5 (2014), pp. 3373–3380.

Acknowledgments

I would like to express my gratitude to Prof. Marco Zannoni and Prof. Paolo Tortora for proposing me this thesis project, entrusting me with the opportunity to represent our institution at Boston University. Their confidence in my abilities has been a source of motivation for the development of this work.

I am grateful to Prof. Paul Withers for hosting me at Boston University and offering invaluable advice throughout this research. Special thanks to Marianna Felici and Drew Coffin, whose precious guidance played a crucial role in shaping this project.

Thanks to everyone in the United States who showed interest in introducing me to their culture. This experience provided a valuable opportunity to broaden my perspectives and open my mind.

Thanks to Andrea Caruso, who provided consistent assistance in my activities from the very beginning of the project until the final editing of this document.

I am profoundly grateful to my family for their unconditional support throughout the years, which was vital for the fulfillment of this achievement.

Last, but not least, thanks to everyone I had the privilege of meeting during my university career. All the experiences we shared enriched this journey in ways I could not have anticipated, making it a memorable chapter of my life.